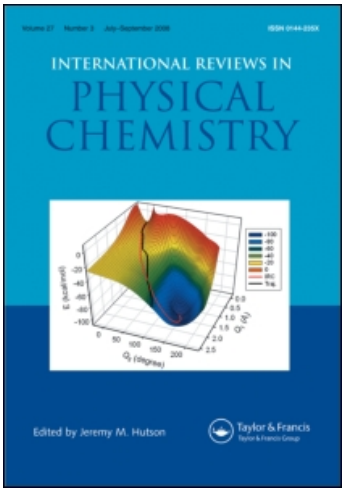

International Reviews in Physical Chemistry
Publication details, including instructions for authors and subscription information:
http://www.informaworld.com/smpp/title~content=t713724383

The plane wave packet approach to quantum scattering theory

Stuart C. Althorpe[a]
[a] Department of Chemistry, University of Exeter, Exeter EX4 4QD, UK

To cite this Article Althorpe, Stuart C.(2004) 'The plane wave packet approach to quantum scattering theory', International Reviews in Physical Chemistry, 23: 2, 219 — 251
To link to this Article: DOI: 10.1080/01442350412331284607
URL: http://dx.doi.org/10.1080/01442350412331284607

INT. REVIEWS IN PHYSICAL CHEMISTRY, 2004
VOL. 23, NO. 2, 219–251

Taylor & Francis
Taylor & Francis Group

The plane wave packet approach to quantum scattering theory

STUART C. ALTHORPE†
Department of Chemistry, University of Exeter, Stocker Road, Exeter EX4 4QD, UK

The Plane Wave Packet (PWP) approach is a new formulation of quantum scattering theory which interprets the results of (energy-domain) scattering experiments in terms of time-evolving wave packets. The wave packets allow one to visualize the scattering of the collision products in space, and thus link the dynamics on the potential surface with the angular distributions measured in experiments. Here we review the theoretical basis of the PWP approach, its connection with conventional quantum scattering theory, and the applications that have been made of it to date. These include calculations on simple model systems, and on the $H + H_2$, $H + D_2$ and $F + HD$ reactions. We give a thorough explanation of the theoretical basis of the PWP approach, which includes a review of the relevant parts of the literature on time-independent reactive scattering. We explain in detail how the PWP approach can be used to separate out different scattering mechanisms, and how such interpretations complement those of time-independent scattering theory. We also suggest possible future developments of the approach.

Contents

† E-mail: s.c.althorpe@exeter.ac.uk

International Reviews in Physical Chemistry ISSN 0144–235X print/ISSN 1366–591X online
http://www.tandf.co.uk/journals
DOI: 10.1080/01442350412331284607

1. Introduction

The Plane Wave Packet (PWP) approach is a recently developed [1–11] formulation of quantum scattering theory, which interprets the results of reactive scattering experiments [1, 9–13] in terms of time-dependent wave packets. The motivation for the approach is to yield for bimolecular reactions the sort of time-evolving pictures that femtosecond spectroscopy [14, 15] yields for unimolecular reactions.[1] The PWP formulation is completely general, and applicable to any bimolecular reaction, or indeed collision between two quantum objects. However, since it requires the solution of the full Schrödinger equation for the reaction dynamics, it is limited computationally to the simple, prototypical, reactions that are often studied using conventional scattering theory [16]. To date, the PWP approach has yielded new insights into the scattering of the $H + D_2$ [1, 2, 8] and $F + HD$ [3, 4] reactions, and into geometric (Berry) phase effects in the $H + H_2$ reaction [5, 6], and is currently being applied to some simple four-atom reactions.

Bimolecular reactions differ from unimolecular reactions in that they are much more directional. Every dynamical event that happens in a bimolecular reaction has reference to the initial approach direction of the reagents. Even when the reaction mechanism is such as to 'forget' this approach direction, this is significant, and characterizes the mechanism as a statistical one. Often, however, the mechanisms 'remember' strongly the approach direction, and there are well characterized examples in the literature [17] of, for example, backward scattering recoil mechanisms, forward scattering glancing mechanisms, and so on. The PWP approach gives a wave packet description of such processes, and therefore describes them as though they were taking place in a femtochemistry experiment. An essential feature of the PWP approach is that, when transformed to the energy domain, the wave packet yields the angular product distributions or *differential cross-sections* (DCSs), which are measured in reactive scattering experiments. The latter [11–13] have seen an impressive increase in the detail and the resolution in which they can measure the DCSs, and sometimes other, yet more detailed, quantities [18]. The PWP method

[1]To our knowledge, no femtochemistry experiment has yet been done on a full bimolecular reaction; the closest to such an experiment are the studies of photoinduced reactions in van der Waals molecules; see e.g. [15].

provides a means of exploiting to the full this data, by providing a rigorous time-dependent interpretation of the DCS which complements the interpretations of conventional scattering theory.

The difference between the PWP approach and conventional scattering theory is not simply that the former is time-dependent, and the latter time-independent. The two approaches also differ in where and when they prepare the reagents and detect the products. Conventional scattering theory [19–21] is effectively the extreme limit of a wave packet theory, in which the spread of energies in the packet tends to zero, and the initial wave packet is prepared in the remote past, with the reagents separated by an asymptotically large distance; the products are detected in the remote future, when they also are separated by an asymptotically large distance. These limits are needed in order to obtain a time-independent 'steady state' description of the reaction. The PWP approach, by contrast, takes no such limits [7]. The reagents are described by a plane wave packet, which contains a finite spread of energies, as would a wave packet prepared in a femtochemistry experiment. The reagents are separated by the smallest distance at which the interaction potential can be neglected (typically 10–20 a.u.). The products are detected at a similar distance, by projecting the time-evolving wave packet on to fixed 'probe' packets (which are also plane waves). Despite the difference between the two approaches, they yield physically equivalent descriptions of the scattering, which can readily be interconverted [7, 8].

Because of this last point, it is possible to obtain the time-evolving wave packets of the PWP approach from time-independent wave functions (and vice versa). Hence it is not necessary to use wave packet methods of solving the Schrödinger equation in order to apply the PWP approach. However, it is usually numerically more efficient to use wave packet methods, since otherwise one would have to repeat a time-independent calculation over a grid of energies. Nevertheless, it is worth bearing in mind that the PWP approach can be used with time-independent methods, if only to clarify that the PWP approach is a method of interpretation, rather than a numerical method of solving the Schrödinger equation. Regarding the latter, there are a variety of excellent methods in the literature [22–29], which could be adapted to implement efficiently the PWP approach.

This review gives a thorough overview of the PWP approach, and pays particular attention to its relation to conventional time-independent scattering theory. In section 2, we summarize the key results of the PWP formulation of scattering theory, for the simplest example of spherical-particle scattering. In section 3, we provide a detailed derivation of the PWP approach, as applied to $A + BC$ reactive scattering. This section is an expanded version of the theory part of ref. [8], and includes extra background material on time-independent $A + BC$ scattering, in order to clarify the relation of the latter to the PWP description. Section 4 ties together the recent applications of the PWP approach, describing the new insights it has yielded into the dynamics of the $H + H_2$, $H + D_2$ and $F + HD$ reactions. It also discusses the best way to implement numerically the PWP approach. In section 5, we suggest possible future developments of the approach, and conclude the review.

2. Key elements of the plane wave packet (PWP) approach

We begin with a summary of the key elements of the plane wave packet (PWP) formulation of quantum scattering. We draw mostly on ref. [7], in which the PWP approach is derived and explained for the simplest case of spherical-particle scattering.

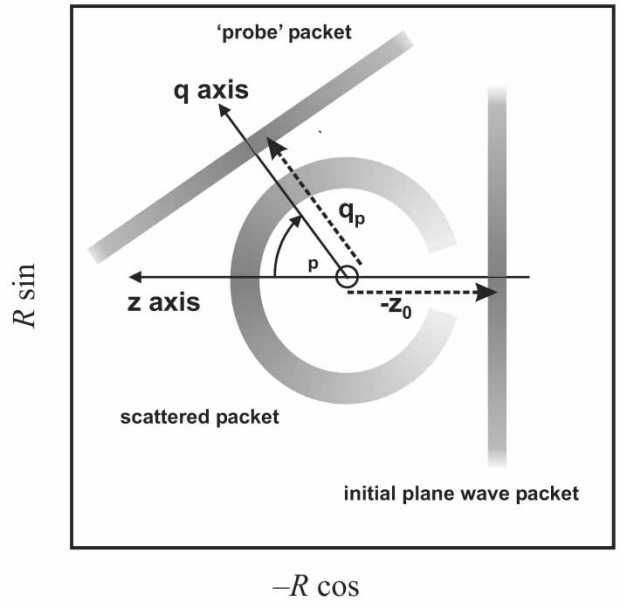

Figure 1. Schematic diagram of the plane wave packet approach, showing a $\phi = 0$ cut through the three-dimensional space in which the particle scatters. The initial plane wave packet is placed at the shortest distance $|z_0|$ from the origin at which the scattering potential can be neglected, and is travelling in the direction of the z-axis. The DCS is obtained by projecting the scattered wave packet on to a series of fixed, plane wave probe packets. One such probe packet is shown, pointing in the direction $\theta = \theta_p$. (Reproduced with permission from ref. [7].)

2.1. *The time-dependent wave packet*

The PWP approach is illustrated schematically in figure 1. The scattering of the particle is described in terms of the usual spherical polar coordinates $\mathbf{R} = (R, \theta, \phi)$, of which R is the distance of the particle from the scattering centre, θ is the scattering angle with respect to the initial approach direction along the z-axis, and ϕ is the azimuthal angle. For spherical-particle scattering, the wave function is symmetric about the z-axis, so the angle ϕ can be dropped. A key assumption [7] behind the PWP approach is that the scattering potential $V(R)$ has a finite range, and may be neglected for $R > R_0$. This assumption could, however, be relaxed, for example to treat charged-particle scattering (by constructing the wave packets from Coulombic functions).

At the initial time $t = 0$, the system is described by a plane wave packet

$$\chi(\mathbf{R}|\overline{k}_o, z_0|0) = A(z - z_0)e^{i\overline{k}_o z}. \tag{1}$$

The packet is travelling in the direction of the positive z-axis, as shown schematically in figure 1. The envelope $A(z - z_0)$ is chosen so as to localize the packet about a negative z distance, as close to the scattering centre as possible, without the packet significantly overlapping the potential. The momentum composition of the packet is given by

$$A(k|\overline{k}_o, z_0) = \frac{1}{2\pi}\int_{-\infty}^{\infty} e^{-ikz}\chi(\mathbf{R}|\overline{k}_o, z_0|0)\,dz \tag{2}$$

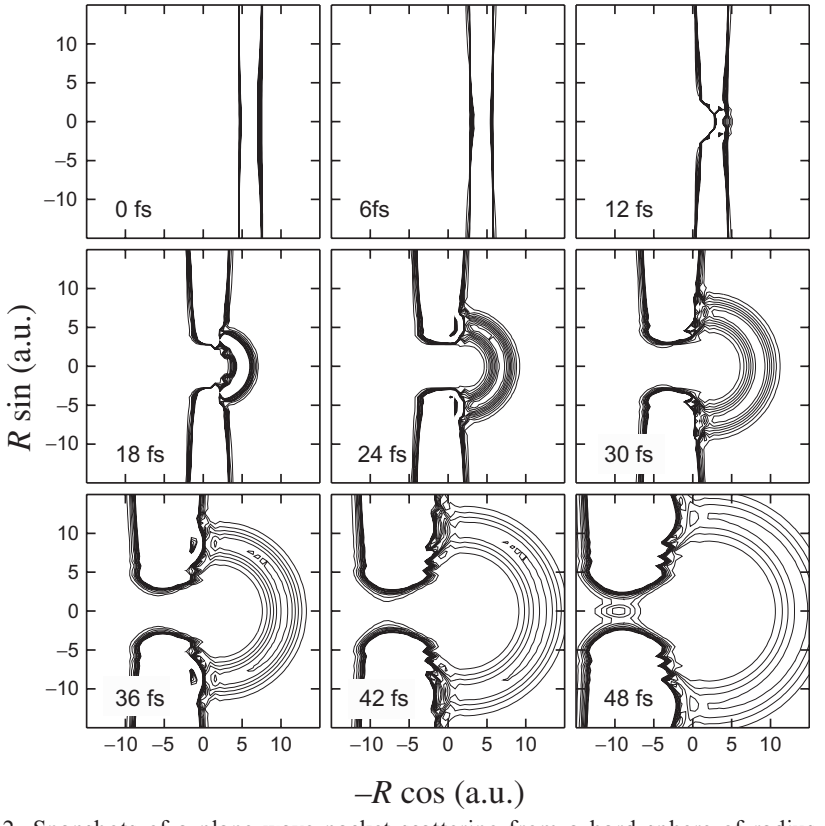

Figure 2. Snapshots of a plane wave packet scattering from a hard sphere of radius 3 a.u. Each snapshot is a $\phi = 0$ cut through $|\chi(\mathbf{R}|\overline{k}_o, z_0|t)|^2 R^2$. (Reproduced with permission from ref. [7].)

and the average momentum in the positive z-direction is $\overline{k}_o\hbar$. The dynamics of the particle at $t > 0$ is described by the time-dependent wave packet

$$\chi(\mathbf{R}|\overline{k}_o, z_0|t) = e^{-i\hat{H}t/\hbar}\chi(\mathbf{R}|\overline{k}_o, z_0|0) \tag{3}$$

where $\hat{H}$ is the hamiltonian.

A simple example of such a wave packet is given in figure 2, which shows a plane wave scattering from a hard sphere. The width of the sphere (not shown) is 3.0 a.u. The well-known 'shadow effect' [21] is evident in the figure at times greater than $t = 24$ fs. This is about as simple a system as one could choose, and gives a clear illustration of why the PWP method is so useful for describing more complex systems. We can see that the scattering is given a clear, physically transparent visualization, which is easy to compare with an intuitive classical picture. Details that show up very well in the wave packet include the development of the diffractive interference pattern in the forward direction, and the off-centre evolution of the backward and sideways scattered 'ring'.

A wave packet such as figure 2 gives a time-dependent description of the scattering in the vicinity of the potential. To compare this description with experiment, one needs to relate the wave packet to the time-independent, asymptotic, description, given by the DCS. To this end, one needs first to relate the wave packet to the

time-independent wave function $\Psi(\mathbf{R}|E)$ of conventional scattering theory [19–21]. This is done by taking the Fourier transform over t, to obtain

$$\xi(\mathbf{R}|\overline{k}_{\mathrm{o}}, z_0|E) = \frac{1}{2\pi\hbar}\int_0^{\infty} \mathrm{e}^{\mathrm{i}Et/\hbar}\chi(\mathbf{R}|\overline{k}_{\mathrm{o}}, z_0|t)\,\mathrm{d}t. \tag{4}$$

The time-independent wave function $\xi(\mathbf{R}|\overline{k}_{\mathrm{o}}, z_0|E)$ is an example of a 'time-independent wave packet' (TIWP) [30], and is the solution of an inhomogeneous form of the time-independent Schrödinger equation. One may show (Appendix A of Ref. [7]) that $\Psi(\mathbf{R}|E)$ is related to $\xi(\mathbf{R}|\overline{k}_{\mathrm{o}}, z_0|E)$ by

$$\Psi(\mathbf{R}|E) = \frac{\hbar^2 k}{mA(k|\overline{k}_{\mathrm{o}}, z_0)}\xi(\mathbf{R}|\overline{k}_{\mathrm{o}}, z_0|E) \tag{5}$$

where m is the mass of the particle, and $\Psi(\mathbf{R}|E)$ satisfies the usual scattering boundary condition [19–21],

$$\Psi(\mathbf{R}|E) \longrightarrow \mathrm{e}^{\mathrm{i}kz} + \frac{f(\theta, E)}{R}\mathrm{e}^{\mathrm{i}kR} \qquad \text{as} \quad R \to \infty. \tag{6}$$

2.2. *Close-up angular distributions*

Before discussing the relation of the wave packet to the DCS, it is useful to stay with the picture of the scattering given by the wave packet, and obtain its angular distribution in the vicinity of the scattering potential. Following ref. [7] we will call this the 'close-up' angular distribution, and will introduce it in its time-dependent form, $\tilde{\sigma}(\theta, t)$, and its time-independent form $\tilde{\sigma}(\theta, E)$. These distributions are taken over a sphere which just encloses the scattering potential. Although they have not been used to date when interpreting chemical reactions, the close-up distributions are potentially very useful, since they can identify separate pieces of scattering, arising from different regions of the potential, which come together and interfere in the DCS.

To obtain the time-dependent distribution $\tilde{\sigma}(\theta, t)$, we take a cut through the wave packet at the angle θ, then calculate the flux of the wave packet normal to a sphere that just encloses the scattering potential. This is done by projecting on to a radial 'probe' packet $\chi(R|\overline{k}_{\mathrm{p}}, R_{\mathrm{p}})/R$, which is localized about $R = R_{\mathrm{p}} > R_0$, and contains a spread of momenta pointing radially outwards, with average momentum $\hbar\overline{k}_{\mathrm{p}}$. The spread of momenta in $\chi(R|\overline{k}_{\mathrm{p}}, R_{\mathrm{p}})$ is chosen to enclose the momenta contained in $A(k|\overline{k}_{\mathrm{o}}, z_0)$ of equation (2). This yields the close-up scattering amplitude

$$\tilde{f}(\theta, t) = \left\langle \chi(\overline{k}_{\mathrm{p}}, R_{\mathrm{p}}) \middle| \chi^{\mathrm{OUT}}(\theta|\overline{k}_{\mathrm{o}}, z_0|t) \right\rangle \tag{7}$$

where we have omitted from $\chi(R|\overline{k}_{\mathrm{p}}, R_{\mathrm{p}})$ and $\chi^{\mathrm{OUT}}(\mathbf{R}|\overline{k}_{\mathrm{o}}, z_0|t)$ the variable R over which we have integrated. (This convention is used throughout the review.) The superscript 'OUT' indicates that the unscattered (i.e. pure plane wave) part of the wave packet has been subtracted from $\chi(\mathbf{R}|\overline{k}_{\mathrm{o}}, z_0|t)$. For example, the $\chi^{\mathrm{OUT}}(\mathbf{R}|\overline{k}_{\mathrm{o}}, z_0|t)$ corresponding to the hard-sphere wave packet of figure 2 is shown in figure 3.

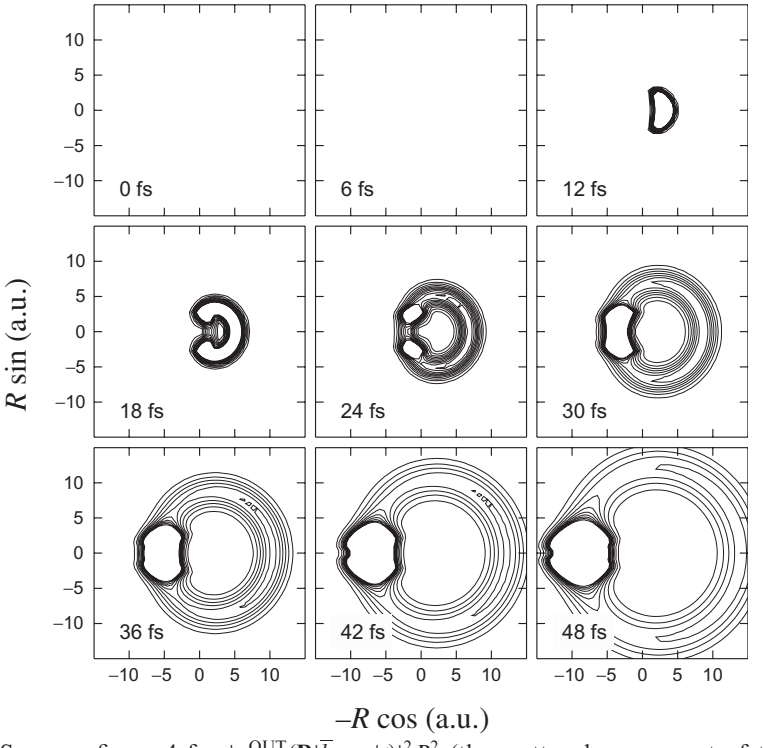

Figure 3. Same as figure 4 for $|\chi^{\mathrm{OUT}}(\mathbf{R}|\overline{k}_{\mathrm{o}}, z_0|t)|^2 R^2$ (the scattered component of the wave packet). (Reproduced with permission from ref. [7].)

The close-up, time-dependent angular distribution is

$$\tilde{\sigma}(\theta, t) = \left|\tilde{f}(\theta, t)\right|^2 \tag{8}$$

and the close-up, time-independent distribution is

$$\tilde{\sigma}(\theta, E) = \left|\tilde{g}(\theta, E)\right|^2 \tag{9}$$

where $\tilde{g}(\theta, E)$ is the time-to-energy Fourier transform of $\tilde{f}(\theta, t)$.

The usefulness of the close-up angular distributions is illustrated by the cut through $\tilde{\sigma}(\theta, E)$, shown in figure 4, which is obtained from the hard-sphere $\chi^{\mathrm{OUT}}(\mathbf{R}|\overline{k}_{\mathrm{o}}, z_0|t)$ shown in figure 3. The most striking difference between $\tilde{\sigma}(\theta, E)$ and the DCS occurs in the forward direction, where the diffractive interference pattern in the latter is completely absent from the close-up distribution. This demonstrates that the interference pattern is not produced at the sphere, but is produced later, as the packet scatters into space. This simple example shows that the close-up angular distributions will probably be useful for disentangling similar interference patterns produced in more complex systems, and would complement existing semiclassical methods of analysis [31].

2.3. *Mapping the wave packet on to the DCS*

We now return to the relation between the wave packet and the DCS, explaining how to map $\chi(\mathbf{R}|\overline{k}_{\mathrm{o}}, z_0|t)$ on to the DCS, so that it can be used directly and

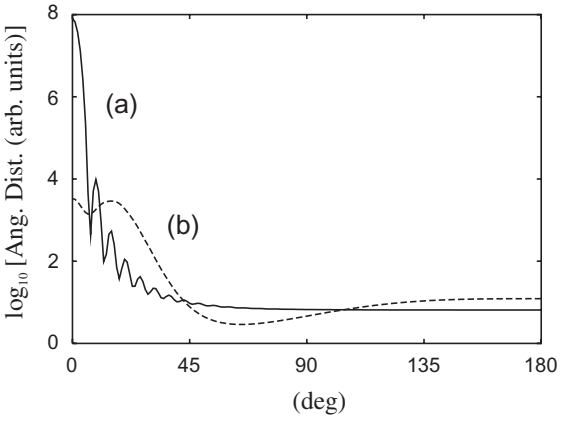

Figure 4. A cut (at $E = 1$ eV) through the time-independent angular distributions obtained from the scattered wave packet of figure 3. Curve (a) is the time-independent DCS $d\sigma/d\Omega(\theta, E)$; curve (b) is the close-up angular distribution $\tilde{\sigma}(\theta, E)$. The curves have been scaled to fit on the same plot. (Reproduced with permission from ref. [7].)

quantitatively to interpret experimental results. The mapping is analogous to a technique which, in electromagnetic wave scattering, is called the 'near-field to far-field' transformation [32, 33]. In the PWP approach [7], the mapping is essentially an application of Newton's first law to the motion of the wave packet for $R > R_0$. It projects out the component of the packet whose momentum vector points in the direction of a given angle θ (and which therefore scatters into this angle in the limit $R \to \infty$). This is done by projecting $\chi^{\mathrm{OUT}}(\mathbf{R}|\overline{k}_{\mathrm{o}}, z_0|t)$ on to a set of probe packets, one of which is illustrated schematically in figure 1. The probe packets are a set of plane wave packets, held tangentially to a sphere of radius R_{p}. Each packet points in a different scattering direction θ_{p}, and has the general form

$$\chi(\mathbf{R}|\theta_{\mathrm{p}}, \overline{k}_{\mathrm{p}}, q_{\mathrm{p}}) = A(q - q_{\mathrm{p}})\, \mathrm{e}^{\mathrm{i}\overline{k}_{\mathrm{p}} q}. \tag{10}$$

The envelope function $A(q - q_{\mathrm{p}})$ is chosen such that $\chi(\mathbf{R}|\theta_{\mathrm{p}}, \overline{k}_{\mathrm{p}}, q_{\mathrm{p}})$ is localized about the distance $q = q_{\mathrm{p}}$ along the q-axis (a vector pointing in the direction of θ_{p}; see figure 1). The spread of $\hbar|k|$ in $\chi(\mathbf{R}|\theta_{\mathrm{p}}, \overline{k}_{\mathrm{p}}, q_{\mathrm{p}})$ must enclose the spread of $\hbar|k|$ in the initial wave packet $\chi(\mathbf{R}|\overline{k}_{\mathrm{o}}, z_0|0)$. Note that probe packets were first used in non-PWP (fixed-J) wave packet calculations, where they are called 'test functions' [34].

The projection on to $\chi(\mathbf{R}|\theta_{\mathrm{p}}, \overline{k}_{\mathrm{p}}, q_{\mathrm{p}})$ effectively 'captures' all those parts of the packet which, in the limit $R \to \infty$, will scatter into $\theta = \theta_{\mathrm{p}}$. It yields the time-dependent scattering amplitude

$$f(\theta_{\mathrm{p}}, t) = \left\langle \chi(\theta_{\mathrm{p}}, \overline{k}_{\mathrm{p}}, q_{\mathrm{p}}) \right| \chi^{\mathrm{OUT}}(\overline{k}_{\mathrm{o}}, z_0|t) \rangle \tag{11}$$

from which we obtain (dropping the 'p' subscripts) the 'time-dependent DCS'[2]

$$\frac{\mathrm{d}\sigma}{\mathrm{d}\Omega}(\theta, t) = \left| f(\theta, t) \right|^2. \tag{12}$$

The time-dependent DCS corresponding to the wave packet of figures 2 and 3 is shown in figure 5. Its main use is to summarize the mapping of the wave packet on to

[2]This time-dependent angular distribution is not strictly a cross-section, but the name seems appropriate given its close relation to the time-independent DCS.

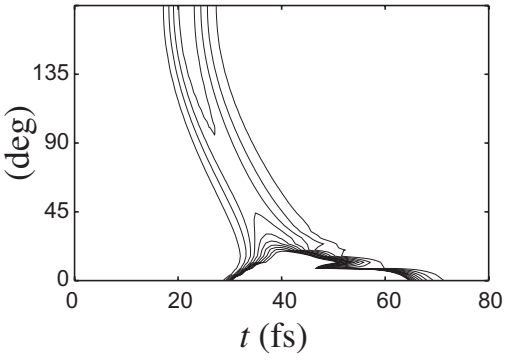

Figure 5. The time-dependent DCS $d\sigma/d\Omega(\theta, t)$, corresponding to the wave packet of figure 3. (Reproduced with permission from Ref. [7].)

the (energy-domain) DCS. The mapping is completed by evaluating the Fourier transform

$$g(\theta, E) = \frac{1}{2\pi\hbar}\int_0^\infty e^{iEt/\hbar} f(\theta, t)\, dt \tag{13}$$

The amplitude $g(\theta, E)$ is proportional to the time-independent scattering amplitude $f(\theta, E)$ of equation (6) according to

$$f(\theta, E) = \frac{g(\theta, E)}{F(\overline{k}_o, z_0, \overline{k}_p, q_p|E)} \tag{14}$$

where $F(\overline{k}_o, z_0, \overline{k}_p, q_p|E)$ is an energy filter [7]. The DCS is obtained from $f(\theta, E)$ using the familiar expression [19–21]

$$\frac{d\sigma}{d\Omega}(\theta, E) = |f(\theta, E)|^2. \tag{15}$$

Thus a time-evolving wave packet, such as the one shown in figure 2, can be mapped rigorously on to the DCS, and used to interpret features in the latter in terms of the time-dependent dynamics on the potential surface. The mapping can be summarized by plotting the time-dependent DCS. For such a simple example as the hard-sphere system, there is little that the wave packet can 'interpret' in the DCS. As one would expect, the wave packet scatters earlier at smaller scattering angles, and the forward peak is spread out in time, and contains interference effects. The more complex systems discussed in the next two sections will show how the mapping of the wave packet on to the DCS gives new insights into the dynamics, which complement those obtained from time-independent scattering.

3. PWP theory for A + BC reactive scattering

This section gives a thorough derivation of the PWP approach for A + BC reactive scattering. This derivation is a more complete version of one published recently [8], augmented to review the relevant parts of the literature for time-independent reactive scattering. The main part of the derivation concerns the relation between the wave packet and the DCS, and is carried out by making a partial wave expansion. This approach is formally equivalent to proving the relation by the application of

Green's theorem (which is how the analogous 'near-field to far-field' transformation is derived in the electromagnetic scattering literature [32, 33]).

3.1. *Atom–rigid-rotor scattering in SF frame*

The main task in applying the PWP approach to treat three-atom reactive scattering is to incorporate the effects of the diatom angular momentum (which couples with the superposition of angular momenta in the plane wave packet). Following Ref. [8], we consider first the case of atom–rigid-rotor scattering, which is the simplest system to incorporate these effects. Here we use the space-fixed (SF) frame for the angular momenta, since this simplifies the derivation. The transformation of these results to the body-fixed (BF) frame (which is often more convenient for describing reactive scattering) is covered in section 3.2.

3.1.1. *Wave packets and time-independent wave functions*

To treat A + BC atom–rigid-rotor scattering, we use the coordinates (γ, α) which orient the diatomic axis in the SF frame. The coordinates $\mathbf{R} = (R, \theta, \phi)$ are the usual A + BC centre-of-mass (CM) scattering coordinates [35–38], with R the length of the A–BC intermolecular axis, and (θ, ϕ) the orientation of this axis in the SF frame. The SF z-axis is the initial A→BC approach direction.

The initial $t = 0$ wave packet has the form [8]

$$\chi^{jm_j}(\mathbf{R}, \gamma, \alpha|0) = \chi(z|\overline{k}_o, z_0|0)\, Y_{jm_j}(\gamma, \alpha) \tag{16}$$

where $\chi(z|\overline{k}_o, z_0|0)$ is a plane wave packet [defined in equation (1)], $Y_{jm_j}(\gamma, \alpha)$ is a spherical harmonic [39], j is the angular momentum quantum number of the BC diatom, and m_j is the projection of j on to the SF z-axis. As in the spherical-particle case, we can neglect the ϕ-dependence (provided we start with AB in one rotational eigenstate, and not a superposition of states). The ensuing collision and scattering dynamics is described by the time-dependent wave packet

$$\chi^{jm_j}(\mathbf{R}, \gamma, \alpha|t) = \mathrm{e}^{-\mathrm{i}\hat{H}t/\hbar}\chi^{jm_j}(\mathbf{R}, \gamma, \alpha|0) \tag{17}$$

where $\hat{H}$ is the full hamiltonian (including the A–BC interaction potential). For clarity, we have simplified the notation by dropping the details of the initial plane wave packet $(\overline{k}_o, z_0)$ from $\chi^{jm_j}(\mathbf{R}, \gamma, \alpha|t)$. These details should always be understood in what follows.

It is useful to separate off the scattered part of the wave packet,

$$\chi^{jm_j\,\mathrm{OUT}}(\mathbf{R}, \gamma, \alpha|t) = \chi^{jm_j}(\mathbf{R}, \gamma, \alpha|t) - \chi^{jm_j\,\mathrm{PW}}(\mathbf{R}, \gamma, \alpha|t) \tag{18}$$

from the unscattered A + BC plane wave packet

$$\chi^{jm_j\,\mathrm{PW}}(\mathbf{R}, \gamma, \alpha|t) = \mathrm{e}^{-\mathrm{i}\hat{H}_0 t/\hbar}\chi^{jm_j}(\mathbf{R}, \gamma, \alpha|0) \tag{19}$$

where H_0 is the hamiltonian for the non-interacting A + BC.

Following section 2.1, we need to relate $\chi^{jm_j}(\mathbf{R}, \gamma, \alpha|t)$ to the time-independent wave function $\Psi^{jm_j}(\mathbf{R}, \gamma, \alpha|E)$. The time-to-energy Fourier transform of $\chi^{jm_j}(\mathbf{R}, \gamma, \alpha|t)$ yields

$$\xi^{jm_j}(\mathbf{R}, \gamma, \alpha|E) = \frac{1}{2\pi\hbar}\int_0^\infty \mathrm{e}^{\mathrm{i}Et/\hbar}\chi^{jm_j}(\mathbf{R}, \gamma, \alpha|t)\,\mathrm{d}t. \tag{20}$$

The function $\xi^{jm_j}(\mathbf{R},\gamma,\alpha|E)$ is a TIWP solution [30], which is a generalization of $\xi(\mathbf{R}|\overline{k}_o,z_0|E)$ of equation (4). In the appendix, we show that

$$\Psi^{jm_j}(\mathbf{R},\gamma,\alpha|E)=\frac{\hbar^2 k_j}{\mu A(k_j|\overline{k}_o,z_0)}\xi^{jm_j}(\mathbf{R},\gamma,\alpha|E) \tag{21}$$

where $A(k_j|\overline{k}_o,z_0)$ is the momentum composition of $\chi(z|\overline{k}_o,z_0|0)$ [defined in equation (2)], μ is the reduced mass associated with motion along the R coordinate, and $k_j=\sqrt{2\mu(E-\epsilon_j)}/\hbar$, with ϵ_j the rotational energy of the diatom. The boundary conditions satisfied by $\Psi^{jm_j}(\mathbf{R},\gamma,\alpha|E)$ in the limit $R\to\infty$ are [35–38]

$$\Psi^{jm_j}(\mathbf{R},\gamma,\alpha|E)\to e^{ik_j z}Y_{jm_j}(\gamma,\alpha)+\frac{1}{R}\sum_{j'm'_j}e^{ik_{j'}R}Y_{j'm'_j}(\gamma,\alpha)f^{jm_j}_{j'm'_j}(\theta,\phi|E) \tag{22}$$

where $f^{jm_j}_{j'm'_j}(\theta,\phi|E)$ is the state-to-state scattering amplitude (from which we can drop the angle ϕ). The DCS is given by

$$\frac{d\sigma_{j'm'_j\leftarrow jm_j}}{d\Omega}(\theta,E)=\frac{k_{j'}}{k_j}\left|f^{jm_j}_{j'm'_j}(\theta,E)\right|^2. \tag{23}$$

3.1.2. *Partial wave expansion*

We now show that there is a direct relation between $\chi^{jm_j\,\mathrm{OUT}}(\mathbf{R},\gamma,\alpha|t)$ and the DCS, which is a generalization of equations (11)–(15). To derive this relation, we expand the wave packets and wave functions in terms of partial waves (eigenfunctions of the total angular momentum operators). The partial wave expansion of the time-independent wave function $\Psi^{jm_j}(\mathbf{R},\gamma,\alpha|E)$ can be written [35–38]

$$\Psi^{jm_j}(\mathbf{R},\gamma,\alpha|E)=\sum_{J=0}^{\infty}\Psi^{jm_j}_J(\mathbf{R},\gamma,\alpha|E) \tag{24}$$

where J is the total angular momentum quantum number. Each partial wave component $\Psi^{jm_j}_J(\mathbf{R},\gamma,\alpha|E)$ can be further expanded, in terms of the basis functions

$$G^{ljM}_J(\theta,\phi;\gamma,\alpha)=\sum_{m m_j}Y_{lm}(\theta,\phi)Y_{jm_j}(\gamma,\alpha)\langle lmjm_j|JM\rangle \tag{25}$$

where l is the end-over-end angular momentum quantum number, $\langle lmjm_j|JM\rangle$ is a Clebsch–Gordan coefficient [39], and M is the projection of J on to the z-axis. For $\Psi^{jm_j\,\mathrm{OUT}}_J(\mathbf{R},\gamma,\alpha|E)$ [defined by expanding $\Psi^{jm_j\,\mathrm{OUT}}(\mathbf{R},\gamma,\alpha|E)$ in analogy with equation (24)], the expansion is [35–38]

$$\Psi^{jm_j\,\mathrm{OUT}}_J(\mathbf{R},\gamma,\alpha|E)=\frac{i\sqrt{\pi}}{k_j R}\sum_{ll'j'}i^l\sqrt{2l+1}\langle l0jm_j|Jm_j\rangle \times G^{l'j'm_j}_J(\theta,\phi;\gamma,\alpha)\Psi^{lj\,\mathrm{OUT}}_{l'j'J}(R|E). \tag{26}$$

The components $\Psi^{lj\,\mathrm{OUT}}_{l'j'J}(R|E)$ satisfy

$$\Psi^{lj\,\mathrm{OUT}}_{l'j'J}(R|E)=\hat{h}^+_{l'}(k_{j'}R)T^{lj}_{l'j'J}(E)\qquad\text{for } R>R_0 \tag{27}$$

where, as in section 2, it is assumed that the scattering potential can be neglected for $R > R_0$. The T-matrix $T^{lj}_{l'j'J}(E)$ is related to the S-matrix by

$$T^{lj}_{l'j'J}(E) = \delta_{ll'}\delta_{jj'} - S^{lj}_{l'j'J}(E). \tag{28}$$

The TIWP solution and the time-dependent wave packets can be expanded in the same fashion:

$$\xi^{jm_j}(\mathbf{R}, \gamma, \alpha|E) = \sum_{J=0}^{\infty} \xi^{jm_j}_J(\mathbf{R}, \gamma, \alpha|E) \tag{29}$$

$$\chi^{jm_j}(\mathbf{R}, \gamma, \alpha|E) = \sum_{J=0}^{\infty} \chi^{jm_j}_J(\mathbf{R}, \gamma, \alpha|E). \tag{30}$$

From the orthogonality of the $G^{ljM}_J(\theta, \phi; \gamma, \alpha)$, we know that, for a given J, the relations between the partial wave components $\chi^{jm_j}_J(\mathbf{R}, \gamma, \alpha|t)$, $\xi^{jm_j}_J(\mathbf{R}, \gamma, \alpha|E)$ and $\Psi^{jm_j}_J(\mathbf{R}, \gamma, \alpha|E)$ are the same as those between the full wave functions, given in equations (20) and (21). Each partial wave packet $\chi^{jm_j}_J(\mathbf{R}, \gamma, \alpha|t)$ satisfies [8]

$$\chi^{jm_j}_J(\mathbf{R}, \gamma, \alpha|t) = \mathrm{e}^{-\mathrm{i}\hat{H}_J t/\hbar} \chi^{jm_j}_J(\mathbf{R}, \gamma, \alpha|0) \tag{31}$$

where $\hat{H}_J$ is the J-dependent hamiltonian for atom–rigid-rotor scattering [35–38]. To work out the form taken by the initial partial wave packets $\chi^{jm_j}_J(\mathbf{R}, \gamma, \alpha|0)$, we use a result of Ref. [7], which is that

$$\chi(z|\overline{k}_o, z_0|0) = \frac{1}{R} \sum_{l=0}^{\infty} \mathrm{i}^l (2l+1) P_l(\cos\theta) \chi_l(R|\overline{k}_o, z_0|0) \tag{32}$$

where

$$\chi_l(R|\overline{k}_o, z_0|0) = \int_{-\infty}^{\infty} \hat{j}_l(kR) \frac{A(k|\overline{k}_o, z_0)}{k} \, \mathrm{d}k \tag{33}$$

and $\hat{j}_l(kR)$ is a Ricatti–Bessel function [19, 20]. The functions $\chi_l(R|\overline{k}_o, z_0|0)$ must in general be computed numerically (except for the $l = 0$ function), and their dependence on l is discussed in Ref. [7]. Using equation (32) to expand $\chi(z|\overline{k}_o, z_0|0)$ in equation (16), and applying the inverse of equation (25), we obtain

$$\chi^{jm_j}_J(\mathbf{R}, \gamma, \alpha|0) = \frac{2\sqrt{\pi}}{R} \sum_{l=|J-j|}^{J+j} \mathrm{i}^l \sqrt{2l+1} \langle l0jm_j|Jm_j\rangle \times G^{ljm_j}_J(\theta, \phi; \gamma, \alpha) \chi_l(R|\overline{k}_o, z_0|0) \tag{34}$$

where, in $G^{ljM}_J(\theta, \phi; \gamma, \alpha)$, we have made the substitution $M = m_j$ (since at $t = 0$ the projection of l on to the z-axis is zero).

3.1.3. *Mapping the wave packet on to the DCS*

To map the wave packet $\chi^{jm_j\,\mathrm{OUT}}(\mathbf{R}, \gamma, \alpha|t)$ on to the state-to-state DCS, one must project out the angular distribution of the velocity vectors contained in the packet, and the rotational eigenstates of the diatom. This is done in analogy with equation (11), by evaluating

$$f^{jm_j}_{j'm'_j}(\theta_p, t) = \left\langle \chi^{j'm'_j}(\theta_p) | \chi^{jm_j\,\mathrm{OUT}}(t) \right\rangle \tag{35}$$

where the probe packets are given by

$$\chi^{j'm'_j}(\mathbf{R},\gamma,\alpha|\theta_p) = \chi(\mathbf{R}|\theta_p,\overline{k}_p,q_p)\,Y_{j'm'_j}(\gamma,\alpha). \tag{36}$$

The plane wave parts of the probe packets, $\chi(\mathbf{R}|\theta_p,\overline{k}_p,q_p)$, were introduced in equation (10). They point in the direction $\theta=\theta_p$ of the q-axis, and are localized about $q=q_p$, with $q_p > R_0$. The function $Y_{j'm'_j}(\gamma,\alpha)$ serves to project out the final rotational state of the diatom. By analogy with section 2, we define the state-to-state time-dependent DCS to be

$$\frac{d\sigma_{j'm'_j\leftarrow jm_j}}{d\Omega}(\theta_p,t) = \left| f^{jm_j}_{j'm'_j}(\theta_p,t)\right|^2 \tag{37}$$

and introduce the time-independent scattering amplitude

$$g^{jm_j}_{j'm'_j}(\theta_p,E) = \frac{1}{2\pi\hbar}\int_0^\infty e^{iEt/\hbar} f^{jm_j}_{j'm'_j}(\theta_p,t)\,dt. \tag{38}$$

Now, referring back to equations (20) and (21), and using equation (35), we can write $g^{jm_j}_{j'm'_j}(\theta_p,E)$ as

$$g^{jm_j}_{j'm'_j}(\theta_p,E) = \frac{\mu A(k_j|\overline{k}_o,z_0)}{\hbar^2 k_j}\left\langle \chi^{j'm'_j}(\theta_p)\,\middle|\,\Psi^{jm_j\,OUT}(E)\right\rangle. \tag{39}$$

We then expand $\Psi^{jm_j\,OUT}(\mathbf{R},\gamma,\alpha|E)$ using equations (24)–(27), and expand the plane wave part of the probe packet as

$$\chi(\mathbf{R}|\theta_p,\overline{k}_p,q_p) = \frac{4\pi}{R}\sum_{l=0}^{\infty}\sum_{m=-l}^{l} i^l\,Y^*_{lm}(\theta_p,0)\,Y_{lm}(\theta,\phi)\,\chi_l(R|\overline{k}_p,q_p). \tag{40}$$

Using the orthogonality of the spherical harmonics, we obtain

$$\begin{aligned}\left\langle \chi^{j'm'_j}(\theta_p)\,\middle|\,\Psi^{jm_j\,OUT}(E)\right\rangle = {}& \frac{4i\pi^{3/2}}{k_j}\\ &\times\sum_{Jll'} i^{l-l'}\sqrt{2l+1}\,Y_{l'm_j-m'_j}(\theta_p,0)\,T^{lj}_{l'j'J}(E)\\ &\times\langle l0jm_j|Jm_j\rangle\left\langle l'm_j-m'_j\,j'm'_j|Jm_j\right\rangle\\ &\times\int_0^\infty \chi^*_{l'}(R|\overline{k}_p,q_p)\hat{h}^+_{l'}(k_{j'}R)\,dR.\end{aligned} \tag{41}$$

The integral on the right is independent of l', and is equal to $i\pi A^*(k_{j'}|\overline{k}_p,q_p)/k_{j'}$ (see Appendix B of Ref. [7]). Hence, dropping the 'p' subscripts, and using the well-known expansion [36–38]

$$\begin{aligned}f^{jm_j}_{j'm'_j}(\theta,E) = \frac{\sqrt{\pi}}{k_j}\sum_{Jll'} {}& i^{l-l'+1}\sqrt{2l+1}\,Y_{l'm_j-m'_j}(\theta,0)\,T^{lj}_{l'j'J}(E)\\ &\times\langle l0jm_j|Jm_j\rangle\left\langle l'm_j-m'_j\,j'm'_j|Jm_j\right\rangle\end{aligned} \tag{42}$$

we obtain

$$f^{jm_j}_{j'm'_j}(\theta,E) = \frac{g^{jm_j}_{j'm'_j}(\theta,E)}{F^{j}_{j'}(\overline{k}_o,z_0,\overline{k}_p,q_p|E)} \tag{43}$$

with

$$F^{j}_{j'}(\overline{k}_{\rm o}, z_0, \overline{k}_{\rm p}, q_{\rm p}|E) = \frac{4\pi^2 {\rm i}\mu}{k_j k_{j'} \hbar^2} A(k_j|\overline{k}_{\rm o}, z_0) A(k_{j'}|\overline{k}_{\rm p}, q_{\rm p})^*. \tag{44}$$

The state-to-state DCS can then be obtained from $f^{jm_j}_{j'm'_j}(\theta, E)$ using equation (23). This is the desired result, that the simple steps outlined in section 2 also apply to the more complicated multichannel case of A + BC rigid-rotor scattering. One can compute the time-evolving wave packet, map it on to the DCS, and illustrate the mapping using the time-dependent DCS.

3.2. *Atom–rigid-rotor scattering in BF frame*

In a practical reactive scattering calculation, the wave packet is often computed in terms of body-fixed (BF) coordinates, in which the intermolecular axis becomes the BF z-axis, and the diatom is oriented within the BF frame, using the angles $(\tilde{\gamma}, \tilde{\alpha})$. Here, we transform the results of the previous section from the SF frame to the BF frame.

3.2.1. *SF to BF transformation*

Before explaining how to implement the plane wave packet method in BF coordinates, we review the SF to BF transformation as it is used in time-independent reactive scattering [35–38]. In place of the SF basis functions $G^{ljM}_J(\theta, \phi; \gamma, \alpha)$, the wave function is expanded in terms of the BF basis functions

$$\tilde{G}^{j\Omega M}_J(\theta, \phi; \tilde{\gamma}, \tilde{\alpha}) = \sqrt{\frac{2J+1}{4\pi}} d^J_{M\Omega}(\theta) {\rm e}^{{\rm i}M\phi} Y_{j\Omega}(\tilde{\gamma}, \tilde{\alpha}) \tag{45}$$

in which $d^J_{M\Omega}(\theta)$ is a reduced Wigner rotation matrix [39] and Ω is the projection on to the BF z-axis of j (which is equal to the projection of J). The transformation between the BF and SF basis functions is

$$\tilde{G}^{j\Omega M}_J(\theta, \phi; \tilde{\gamma}, \tilde{\alpha}) = \sum_l C(l, j, \Omega|J) G^{ljM}_J(\theta, \phi; \gamma, \alpha) \tag{46}$$

where

$$C(l, j, \Omega|J) = \sqrt{\frac{2l+1}{2J+1}} \langle l0j\Omega|J\Omega\rangle. \tag{47}$$

When re-expressed in terms of BF coordinates, the time-independent wave function $\Psi^{jm_j}(\mathbf{R}, \gamma, \alpha|E)$ becomes $\Psi^{j\kappa}(\mathbf{R}, \tilde{\gamma}, \tilde{\alpha}|E)$. The quantum number κ is the projection of j on to the A→BC approach velocity vector. This vector points in the same direction as the SF z-axis, and in the opposite direction to the BF z-axis, so that $\kappa = m_j = -\Omega$. The scattered part of the wave function, $\Psi^{j\kappa\,{\rm OUT}}(\mathbf{R}, \tilde{\gamma}, \tilde{\alpha}|E)$, satisfies the boundary conditions [35–38]

$$\Psi^{j\kappa\,{\rm OUT}}(\mathbf{R}, \tilde{\gamma}, \tilde{\alpha}|E) \longrightarrow \frac{1}{R} \sum_{j'\kappa'} {\rm e}^{{\rm i}k_{j'}R} Y_{j'\kappa'}(\tilde{\gamma}, \tilde{\alpha}) f^{j\kappa}_{j'\kappa'}(\theta, \phi|E) \tag{48}$$

in the limit $R \to \infty$.

One can expand $\Psi^{j\kappa\,\mathrm{OUT}}(\mathbf{R},\tilde{\gamma},\tilde{\alpha}|E)$ in terms of partial waves [in analogy with equation (24)], and each partial wave component $\Psi_J^{j\kappa\,\mathrm{OUT}}(\mathbf{R},\tilde{\gamma},\tilde{\alpha}|E)$ can be further expanded as

$$\Psi_J^{j\kappa\,\mathrm{OUT}}(\mathbf{R},\tilde{\gamma},\tilde{\alpha}|E)=\frac{\mathrm{i}}{2k_jR}\sum_{j'\Omega'}(2J+1)d^J_{\kappa\Omega'}(\theta)\mathrm{e}^{\mathrm{i}\kappa\phi}Y_{j\Omega'}(\tilde{\gamma},\tilde{\alpha})\Psi^{j\kappa\,\mathrm{OUT}}_{j'\Omega'J}(R|E). \tag{49}$$

In the limit $R\to\infty$, the BF z-axis lines up with the A$\rightarrow$BC velocity vector (since the A + BC appears to be scattering from a distant point), with the result that $\Omega'\to\kappa'$. Thus the components $\Psi^{j\kappa\,\mathrm{OUT}}_{j'\Omega'J}(R|E)$ satisfy

$$\Psi^{j\kappa\,\mathrm{OUT}}_{j'\Omega'J}(R|E)\longrightarrow\Psi^{j\kappa\,\mathrm{OUT}}_{j'\kappa'J}(R|E)=\mathrm{e}^{\mathrm{i}k_jR}T^{j\kappa}_{j'\kappa'J}(E) \tag{50}$$

where

$$T^{j\kappa}_{j'\kappa'J}(E)=\sum_{ll'}C(l,j,-\kappa|J)C(l',j',\kappa'|J)\mathrm{i}^{l-l'}T^{lj}_{l'j'J}(E) \tag{51}$$

is the BF T-matrix. The latter can be used to construct the BF state-to-state scattering amplitude using

$$f^{j\kappa}_{j'\kappa'}(\theta,E)=\frac{\mathrm{i}}{2k_j}\sum_J(2J+1)d^J_{\kappa\kappa'}(\theta)T^{j\kappa}_{j'\kappa'J}(E) \tag{52}$$

where we have set $\phi=0$. The BF state-to-state DCS is given by [35–38]

$$\frac{\mathrm{d}\sigma_{j'\kappa'\leftarrow j\kappa}}{\mathrm{d}\Omega}(\theta,E)=\frac{k_{j'}}{k_j}\left|f^{j\kappa}_{j'\kappa'}(\theta,E)\right|^2. \tag{53}$$

3.2.2. *PWP theory in BF frame*

The wave packet $\chi^{jm_j}(\mathbf{R},\gamma,\alpha|t)$ can be re-expressed in BF coordinates, and written $\chi^{j\kappa}(\mathbf{R},\tilde{\gamma},\tilde{\alpha}|t)$, where $\kappa=m_j$ (since, as for the time-independent wave function, the initial velocity vector points along the SF z-axis). Expressing equation (16) in BF coordinates, gives the following expression for the initial wave packet

$$\chi^{j\kappa}(\mathbf{R},\tilde{\gamma},\tilde{\alpha}|0)=\chi(z|\overline{k}_\mathrm{o},z_0|0)\sum_\Omega d^j_{\kappa\Omega}(\theta)\mathrm{e}^{\mathrm{i}\kappa\phi}Y_{j\Omega}(\tilde{\gamma},\tilde{\alpha}). \tag{54}$$

In contrast to the time-independent wave function, we no longer have $\Omega=-\kappa$. This is because $\chi(z|\overline{k}_\mathrm{o},z_0|0)$ spreads over a range of θ, and hence the BF axes of the BC diatoms are pointing in a range of directions. Only the BC diatoms for which $\theta=\pi$ (i.e. those centred on the z-axis) satisfy $\Omega=-\kappa$.

Because $\chi^{j\kappa}(\mathbf{R},\tilde{\gamma},\tilde{\alpha}|t)$ and $\Psi^{j\kappa}(\mathbf{R},\tilde{\gamma},\tilde{\alpha}|E)$ are simply the SF functions of section 3.1, re-expressed in BF coordinates, we know that they must satisfy equations (17)–(21). In particular, we can define the BF version of the TIWP, $\xi^{j\kappa}(\mathbf{R},\tilde{\gamma},\tilde{\alpha}|E)$, in analogy with equation (20), and we know that this function is proportional to $\Psi^{j\kappa}(\mathbf{R},\tilde{\gamma},\tilde{\alpha}|E)$, according to equation (21). By analogy with equation (30), we can expand the BF wave packet as a sum over partial wave packets $\chi^{j\kappa}_J(\mathbf{R},\tilde{\gamma},\tilde{\alpha}|t)$. To obtain the form of the partial wave initial packets, we substitute the inverse of equation (46) into equation (34), which gives

$$\chi^{j\kappa}_J(\mathbf{R},\tilde{\gamma},\tilde{\alpha}|0)=\frac{1}{R}\sum_\Omega d^J_{\kappa\Omega}(\theta)\mathrm{e}^{\mathrm{i}\kappa\phi}Y_{j\Omega}(\tilde{\gamma},\tilde{\alpha})\chi^{j\kappa\Omega}_J(R|\overline{k}_\mathrm{o},z_0|0) \tag{55}$$

where

$$\chi_J^{j\kappa\Omega}(R|\overline{k}_o, z_0|0) = \sum_l (2l+1)\langle l0j\kappa|J\kappa\rangle \times \langle l0j\Omega|J\Omega\rangle i^l \chi_l(R|\overline{k}_o, z_0|0). \tag{56}$$

To map the wave packet $\chi^{j\kappa}(\mathbf{R}, \tilde{\gamma}, \tilde{\alpha}|t)$ on to the state-to-state DCS, we project on to probe wave packets of the form

$$\chi^{j'\kappa'}(\mathbf{R}, \tilde{\gamma}, \tilde{\alpha}|\theta_p) = \chi(\mathbf{R}|\theta_p, \overline{k}_p, q_p) W^{j'\kappa'}(\theta, \phi, \tilde{\gamma}, \tilde{\alpha}|\theta_p). \tag{57}$$

The function $\chi(\mathbf{R}|\theta_p, \overline{k}_p, q_p)$ is a plane wave packet identical to that used in the SF probe of equation (36). The rotational function $W^{j'\kappa'}(\theta, \phi, \tilde{\gamma}, \tilde{\alpha}|\theta_p)$ serves to project out the rotational eigenstate $|j'\kappa'\rangle$, where κ' is the projection of j' on to the q-axis (which points in the direction $\theta = \theta_p$). The form of $W^{j'\kappa'}(\theta, \phi, \tilde{\gamma}, \tilde{\alpha}|\theta_p)$ is [8]

$$W^{j'\kappa'}(\theta, \phi, \tilde{\gamma}, \tilde{\alpha}|\theta_p) = \sum_{\Omega'} R_{\Omega'}^{j'\kappa'}(\theta_p, \theta, \phi) Y_{j'\Omega'}(\tilde{\gamma}, \tilde{\alpha}) \tag{58}$$

where the rotation operator $R_{\Omega'}^{j'\kappa'}(\theta_p, \theta, \phi)$ is

$$R_{\Omega'}^{j'\kappa'}(\theta_p, \theta, \phi) = \sum_{m_j'} d^{j'}_{m_j'\kappa'}(\theta_p) d^{j'}_{m_j'\Omega'}(\theta) e^{im_j'\phi}. \tag{59}$$

Note that the dependence of $W^{j'\kappa'}(\theta, \phi, \tilde{\gamma}, \tilde{\alpha}|\theta_p)$ upon (θ, ϕ) means that one must take care to project out $|j'\kappa'\rangle$ before projecting on to the plane wave packet $\chi(\mathbf{R}|\theta_p, \overline{k}_p, q_p)$. In other words, before projecting on to the plane wave packet, one must line up the axes of quantization of the diatoms so that they all point in the direction $\theta = \theta_p$.

The projection on to the probe packets yields the BF, time-dependent scattering amplitude

$$f_{j'\kappa'}^{j\kappa}(\theta_p, t) = \langle \chi^{j'\kappa'}(\theta_p)|\chi^{j\kappa\,\mathrm{OUT}}(t)\rangle. \tag{60}$$

By analogy with section 2, we define the time-dependent DCS

$$\frac{d\sigma_{j'\kappa'\leftarrow j\kappa}}{d\Omega}(\theta, t) = \left| f_{j'\kappa'}^{j\kappa}(\theta, t) \right|^2 \tag{61}$$

and the time-independent scattering amplitude

$$g_{j'\kappa'}^{j\kappa}(\theta, E) = \frac{1}{2\pi\hbar} \int_0^\infty e^{iEt/\hbar} f_{j'\kappa'}^{j\kappa}(\theta, t)\, dt. \tag{62}$$

By applying equations (39)–(44), and using some angular momentum algebra to convert to the BF frame,[3] one can show that

$$f_{j'\kappa'}^{j\kappa}(\theta, E) = \frac{g_{j'\kappa'}^{j\kappa}(\theta, E)}{F_{j'}^{j}(\overline{k}_o, z_0, \overline{k}_p, q_p|E)} \tag{63}$$

where $f_{j'\kappa'}^{j\kappa}(\theta, E)$ is the standard, time-independent scattering amplitude, which yields the state-to-state DCS via equation (53). Hence the relation between the wave packet and the DCS is almost as simple and direct in the BF frame as in the SF frame

[3] The algebra required is not difficult, but is lengthy, and includes two applications of the Clebsch–Gordan series [39]. It is left as an exercise for the reader.

(section 3.1). The only additional step required is to rotate the quantization axis of the BC angular momentum so that it lines up with the q-axis of each probe packet.

3.3. *Full A + BC rearrangement scattering*

It is straightforward to generalize the forgoing to treat A + BC reactive scattering, since including the extra degrees of freedom (i.e. allowing the diatomic bond length to vary, and allowing rearrangement to AC + B and AB + C) does not complicate the simple mapping between the wave packet and the DCS. We derive here the key equations obtained by generalizing the results of section 3.2, starting with a review of the essential results from the time-independent treatment of A + BC reactive scattering [36–38, 40].

3.3.1. *Conventional time-independent formulation*

To describe A + BC reactive scattering, one must take into account the three possible arrangements of the atoms. We label these with the parameter λ, where $\lambda =$ 1 (A + BC), 2 (AC + B), or 3 (AB + C). One can define three sets of coordinates $(\mathbf{R}_\lambda, \tilde{\gamma}_\lambda, \tilde{\alpha}_\lambda, r_\lambda)$, each adapted to one particular arrangement [38, 40]. For example, when λ=1 we have the BF coordinates of section 3.2, plus the additional coordinate r_λ, which is the BC bond length. Taken together, the coordinates $(R_\lambda, \tilde{\gamma}_\lambda, r_\lambda)$ are the BF Jacobi coordinates [38, 40], defined with respect to arrangement λ. The three sets of scattering angles $(\theta_\lambda, \phi_\lambda)$, are defined with respect to a common SF z-axis, which is taken to be the reagent approach direction.

The time-independent wave function $\Psi^{n\kappa}(\mathbf{R}_\lambda, \tilde{\gamma}_\lambda, \tilde{\alpha}_\lambda, r_\lambda|E)$ satisfies the boundary conditions [36–38, 40]

$$\Psi^{n\kappa\,\mathrm{OUT}}(\mathbf{R}_\lambda, \tilde{\gamma}_\lambda, \tilde{\alpha}_\lambda, r_\lambda|E) \longrightarrow \sum_{n'\kappa'} \frac{1}{R_{\lambda'}} \mathrm{e}^{\mathrm{i}k_{n'}R} Y_{j'\kappa'}(\tilde{\gamma}_{\lambda'}, \tilde{\alpha}_{\lambda'}) \Phi_{n'}(r_{\lambda'}) f^{j\kappa}_{j'\kappa'}(\theta_{\lambda'}, \phi_{\lambda'}|E) \qquad (64)$$

in the limits $R_{\lambda'} \to \infty$ ($\lambda' = 1, 2, 3$). This equation is essentially equation (48), generalized to include the three product arrangements $\lambda' = 1, 2, 3$, and the diatom vibrational wave functions $\Phi_{n'}(r_{\lambda'})$. The label n refers collectively to the quantum numbers $\{jv\lambda\}$ of the reagents; n' refers to the quantum numbers $\{j'v'\lambda'\}$ of the products. As in section 3.2, κ is the projection of j on to the approach velocity of the reagent; κ' is the projection of j' on to the velocity of the products (in a given arrangement λ'). The momentum associated with the nth channel is $\hbar k_n = \sqrt{2\mu_\lambda(E - \epsilon_n)}$, where μ_λ is the reduced mass associated with motion along R_λ, and ϵ_n is the rovibrational energy level of the diatom. On the right-hand side of equation (64), each arrangement λ' is represented in terms of the coordinates adapted to that value of λ'. Thus it is assumed that, when representing $\Psi^{n\kappa}(\mathbf{R}_\lambda, \tilde{\gamma}_\lambda, \tilde{\alpha}_\lambda, r_\lambda|E)$, one can switch between the three sets of coordinates (using, say, numerical interpolation [27, 38], or a hyperspherical coordinate system [40, 41]).

By analogy with equation (24), one can expand $\Psi^{n\kappa}(\mathbf{R}_\lambda, \tilde{\gamma}_\lambda, \tilde{\alpha}_\lambda, r_\lambda|E)$ as a sum over J:

$$\Psi^{n\kappa}(\mathbf{R}_\lambda, \tilde{\gamma}_\lambda, \tilde{\alpha}_\lambda, r_\lambda|E) = \sum_{J=0}^{\infty} \Psi^{n\kappa}_J(\mathbf{R}_\lambda, \tilde{\gamma}_\lambda, \tilde{\alpha}_\lambda, r_\lambda|E). \qquad (65)$$

Each partial wave component $\Psi_J^{n\kappa}(\mathbf{R}_\lambda, \tilde{\gamma}_\lambda, \tilde{\alpha}_\lambda, r_\lambda|E)$ can be further expanded in terms of the basis functions

$$\mathcal{Y}_J^{n\Omega M}(\theta_\lambda, \phi_\lambda; \tilde{\gamma}_\lambda, \tilde{\alpha}_\lambda; r_\lambda) = \tilde{G}_J^{j\Omega M}(\theta_\lambda, \phi_\lambda; \tilde{\gamma}_\lambda, \tilde{\alpha}_\lambda)\Phi_n(r_\lambda) \tag{66}$$

where the $\tilde{G}_J^{j\Omega M}(\theta_\lambda, \phi_\lambda; \tilde{\gamma}_\lambda, \tilde{\alpha}_\lambda)$ are defined in equation (45). This gives [36–38]

$$\begin{aligned}\Psi_J^{n\kappa\,\mathrm{OUT}}(\mathbf{R}_\lambda, \tilde{\gamma}_\lambda, \tilde{\alpha}_\lambda, r_\lambda|E) = \frac{\mathrm{i}}{2k_n}\sum_{n'\Omega'}\frac{1}{R_{\lambda'}}(2J+1)d^J_{\kappa\Omega'}(\theta_{\lambda'})\mathrm{e}^{\mathrm{i}\kappa\phi_{\lambda'}}Y_{j'\Omega'}(\tilde{\gamma}_{\lambda'}, \tilde{\alpha}_{\lambda'}) \\ \times \Phi_{n'}(r_{\lambda'})\Psi^{n\kappa\,\mathrm{OUT}}_{n'\Omega'J}(R_{\lambda'}|E)\end{aligned} \tag{67}$$

which is an obvious generalization of equation (49). In the limits $R_{\lambda'} \to \infty$, the components $\Psi^{n\kappa\,\mathrm{OUT}}_{n'\Omega'J}(R_{\lambda'}|E)$ satisfy

$$\Psi^{n\kappa\,\mathrm{OUT}}_{n'\Omega'J}(R_{\lambda'}|E) \longrightarrow \Psi^{n\kappa\,\mathrm{OUT}}_{n'\kappa'J}(R_{\lambda'}|E) = \mathrm{e}^{\mathrm{i}k_{n'}R_{\lambda'}}T^{n\kappa}_{n'\kappa'J}(E) \tag{68}$$

where the T-matrix is related to the S-matrix by

$$T^{n\kappa}_{n'\kappa'J}(E) = \delta_{nn'}\delta_{\kappa\kappa'} - S^{n\kappa}_{n'\kappa'J}(E). \tag{69}$$

The inelastic ($\lambda' = \lambda$) and reactive ($\lambda' \neq \lambda$) scattering amplitudes are given by

$$f^{n\kappa}_{n'\kappa'}(\theta, E) = \frac{\mathrm{i}}{2k_n}\sum_J(2J+1)d^J_{\kappa\kappa'}(\theta)T^{n\kappa}_{n'\kappa'J}(E) \tag{70}$$

where the λ' subscript has been dropped from $\theta_{\lambda'}$ (since it is unambiguous which of the three scattering angles is intended). The state-to-state DCS is obtained from [36–38]

$$\frac{\mathrm{d}\sigma_{n'\kappa'\leftarrow n\kappa}}{\mathrm{d}\Omega}(\theta, E) = \frac{\mu_\lambda k_{n'}}{\mu_{\lambda'}k_n}\left|f^{n\kappa}_{n'\kappa'}(\theta, E)\right|^2. \tag{71}$$

3.3.2. *PWP formulation*

Extension of the PWP approach to reactive A + BC scattering is straightforward. The time-evolving wave packet is now a function of the arrangement coordinates just described, and may be written $\chi^{n\kappa}(\mathbf{R}_\lambda, \tilde{\gamma}_\lambda, \tilde{\alpha}_\lambda, r_\lambda|t)$. The initial $t = 0$ wave packet is given by

$$\chi^{n\kappa}(\mathbf{R}_\lambda, \tilde{\gamma}_\lambda, \tilde{\alpha}_\lambda, r_\lambda|0) = \chi^{j\kappa}(\mathbf{R}_\lambda, \tilde{\gamma}_\lambda, \tilde{\alpha}_\lambda|0)\Phi_n(r_\lambda) \tag{72}$$

where $\chi^{j\kappa}(\mathbf{R}_\lambda, \tilde{\gamma}_\lambda, \tilde{\alpha}_\lambda|0)$ is defined in equation (54). As with the time-independent wave function, it is assumed that one can switch between the three sets of coordinates $(\mathbf{R}_\lambda, \tilde{\gamma}_\lambda, \tilde{\alpha}_\lambda, r_\lambda)$, and that the wave packet in arrangement λ is represented in terms of coordinates adapted to that arrangement. As above, we assume that the interaction potential extends for a finite range, such that it can be neglected for $R_\lambda > R_0$. Hence $\chi^{n\kappa}(\mathbf{R}_\lambda, \tilde{\gamma}_\lambda, \tilde{\alpha}_\lambda, r_\lambda|0)$ describes the reactive collision on and close to the scattering potential.

By analogy with equation (20), we can take the time-to-energy Fourier transform of $\chi^{n\kappa}(\mathbf{R}_\lambda, \tilde{\gamma}_\lambda, \tilde{\alpha}_\lambda, r_\lambda|t)$ to obtain the TIWP solution

$$\xi^{n\kappa}(\mathbf{R}_\lambda, \tilde{\gamma}_\lambda, \tilde{\alpha}_\lambda, r_\lambda|E) = \frac{1}{2\pi\hbar}\int_0^\infty \mathrm{e}^{\mathrm{i}Et/\hbar}\chi^{n\kappa}(\mathbf{R}_\lambda, \tilde{\gamma}_\lambda, \tilde{\alpha}_\lambda, r_\lambda|t)\,\mathrm{d}t. \tag{73}$$

One can generalize equation (21) (see the appendix) so as to obtain the relation

$$\Psi^{n\kappa}(\mathbf{R}_\lambda, \tilde{\gamma}_\lambda, \tilde{\alpha}_\lambda, r_\lambda|E) = \frac{\hbar^2 k_n}{\mu_\lambda A(k_n|\bar{k}_o, z_0)} \xi^{n\kappa}(\mathbf{R}_\lambda, \tilde{\gamma}_\lambda, \tilde{\alpha}_\lambda, r_\lambda|E) \tag{74}$$

between the time-independent wave function and the TIWP. Both the time-dependent wave packet and the TIWP can be expanded as a sum over J:

$$\chi^{n\kappa}(\mathbf{R}_\lambda, \tilde{\gamma}_\lambda, \tilde{\alpha}_\lambda, r_\lambda|t) = \sum_{J=0}^{\infty} \chi_J^{n\kappa}(\mathbf{R}_\lambda, \tilde{\gamma}_\lambda, \tilde{\alpha}_\lambda, r_\lambda|t) \tag{75}$$

$$\xi^{n\kappa}(\mathbf{R}_\lambda, \tilde{\gamma}_\lambda, \tilde{\alpha}_\lambda, r_\lambda|E) = \sum_{J=0}^{\infty} \xi_J^{n\kappa}(\mathbf{R}_\lambda, \tilde{\gamma}_\lambda, \tilde{\alpha}_\lambda, r_\lambda|E) \tag{76}$$

and the partial wave components can be further expanded in terms of the basis functions $\mathcal{Y}_J^{n\Omega M}(\theta_\lambda, \phi_\lambda; \tilde{\gamma}_\lambda, \tilde{\alpha}_\lambda; r_\lambda)$ of equation (66).

To relate the wave packet $\chi^{n\kappa}(\mathbf{R}_\lambda, \tilde{\gamma}_\lambda, \tilde{\alpha}_\lambda, r_\lambda|t)$ to the DCS, one projects on to probe packets of the form

$$\chi^{n'\kappa'}(\mathbf{R}_{\lambda'}, \tilde{\gamma}_{\lambda'}, \tilde{\alpha}_{\lambda'}, r_{\lambda'}|\theta_p) = \chi^{j'\kappa'}(\mathbf{R}_{\lambda'}, \tilde{\gamma}_{\lambda'}, \tilde{\alpha}_{\lambda'}|\theta_p)\Phi_{n'}(r_{\lambda'}) \tag{77}$$

where $\chi^{j'\kappa'}(\mathbf{R}_{\lambda'}, \tilde{\gamma}_{\lambda'}, \tilde{\alpha}_{\lambda'}|\theta_p)$ is defined in equation (57). Hence the only complication over the BF rigid-rotor case of section 3.2 is that one must project out the vibrational eigenstates, and repeat the projections for each value of λ'. The projections yield the state-to-state, time-dependent scattering amplitudes

$$f_{n'\kappa'}^{n\kappa}(\theta_p, t) = \langle \chi^{n'\kappa'}(\theta_p)|\chi^{n\kappa\,\mathrm{OUT}}(t)\rangle. \tag{78}$$

Following section 3.2, we define the time-dependent DCS

$$\frac{d\sigma_{n'\kappa'\leftarrow n\kappa}}{d\Omega}(\theta, t) = \left|f_{n'\kappa'}^{n\kappa}(\theta, t)\right|^2 \tag{79}$$

and the time-independent scattering amplitude

$$g_{n'\kappa'}^{n\kappa}(\theta, E) = \frac{1}{2\pi\hbar}\int_0^\infty e^{iEt/\hbar} f_{n'\kappa'}^{n\kappa}(\theta, t)\, dt. \tag{80}$$

We can use equations (73) and (74) to write the latter as

$$g_{n'\kappa'}^{n\kappa}(\theta, E) = \frac{\mu_\lambda A(k_n|\bar{k}_o, z_0)}{\hbar^2 k_n}\langle \chi^{n'\kappa'}(\theta_p)|\Psi^{n\kappa\,\mathrm{OUT}}(E)\rangle \tag{81}$$

and can then expand $\Psi^{n\kappa\,\mathrm{OUT}}(\mathbf{R}_\lambda, \tilde{\gamma}_\lambda, \tilde{\alpha}_\lambda, r_\lambda|E)$ using equations (65) and (67), and expand the plane wave part of the probe packet using equation (40). This gives an expression which, when transformed to the SF frame,[4] yields a generalized version of equation (41), from which one obtains the relation

$$f_{n'\kappa'}^{n\kappa}(\theta, E) = \frac{g_{n'\kappa'}^{n\kappa}(\theta, E)}{F_{n'}^{n}(\bar{k}_o, z_0, \bar{k}_p, q_p|E)} \tag{82}$$

[4]The algebra required is not difficult, but is lengthy, and includes two applications of the Clebsch–Gordan series [39]. It is left as an exercise for the reader.

with

$$F^{n}_{n'}(\overline{k}_{\rm o}, z_0, \overline{k}_{\rm p}, q_{\rm p}|E) = \frac{4\pi^2 {\rm i}\mu_\lambda}{k_n k_{n'}\hbar^2} A(k_n|\overline{k}_{\rm o}, z_0) A(k_{n'}|\overline{k}_{\rm p}, q_{\rm p})^*. \tag{83}$$

Having obtained $f^{n\kappa}_{n'\kappa'}(\theta, E)$, one can calculate the DCS using equation (71). This completes the derivation of the PWP formulation for atom-plus-diatom reactive scattering, and its relation to the conventional time-independent treatment of these systems. The same simple relation between the time-evolving wave packet and the DCS holds for A + BC reactive scattering, as for atom–rigid-rotor scattering. Hence one can use the PWP approach to interpret the DCS (measured in a reactive scattering experiment) in terms of the time-evolution of the wave packet $\chi^{n\kappa}(\mathbf{R}_\lambda, \tilde{\gamma}_\lambda, \tilde{\alpha}_\lambda, r_\lambda|t)$.

4. Implementation and examples

The PWP approach has now been applied numerically to a range of A + BC reactions, including the prototypical H + D_2 [1, 2, 8] and F + HD [3, 4] reactions; these applications are reviewed in some detail in sections 4.2–4.4. Section 4.1 explains the general numerical strategy used when applying the PWP approach.

4.1. *Overall strategy*

One might think that the formulae of section 3 could be used as the basis of a numerical method for solving the time-dependent Schrödinger equation describing the motion of the nuclei. Probably such a method could be devised, but it would be numerically inefficient, for reasons which are summarized in refs. [7] and [8]. Instead, we apply the formulae of section 3 indirectly. The overall strategy [8] is to compute the time-independent wave functions $\Psi^{n\kappa}_J(\mathbf{R}_\lambda, \tilde{\gamma}_\lambda, \tilde{\alpha}_\lambda, r_\lambda|E)$, over a grid of E values. We then recover the $\xi^{n\kappa}_J(\mathbf{R}_\lambda, \tilde{\gamma}_\lambda, \tilde{\alpha}_\lambda, r_\lambda|E)$ from equation (74), and compute the wave packet $\chi^{n\kappa}_J(\mathbf{R}_\lambda, \tilde{\gamma}_\lambda, \tilde{\alpha}_\lambda, r_\lambda|t)$ by evaluating the inverse of equation (73). The time-dependent DCS is obtained in a similar manner, by computing the time-independent scattering amplitude $f^{n\kappa}_{n'\kappa'}(\theta, E)$ over a grid of E values, converting it to $g^{n\kappa}_{n'\kappa'}(\theta, E)$ using equation (82), and obtaining $f^{n\kappa}_{n'\kappa'}(\theta, t)$ from the inverse of equation (80).

One advantage of this approach is that one may apply equations (74) and (82) any number of times, using different energy filters. This aspect is discussed in section 4.3.2 below. The time-independent quantities $\Psi^{n\kappa}_J(\mathbf{R}_\lambda, \tilde{\gamma}_\lambda, \tilde{\alpha}_\lambda, r_\lambda|E)$ and $f^{n\kappa}_{n'\kappa'}(\theta, E)$ could, in principle, be computed using a standard coupled-channel method [42–44] of solving the time-independent Schrödinger equation. However, since the calculations need to be repeated over a grid of E values, and since the wave function is required as a function of the coordinates, it is usually more efficient to obtain $\Psi^{n\kappa}_J(\mathbf{R}_\lambda, \tilde{\gamma}_\lambda, \tilde{\alpha}_\lambda, r_\lambda|E)$ and $f^{n\kappa}_{n'\kappa'}(\theta, E)$ from a series of fixed-J, wave packet calculations [8, 27] (which propagate Gaussian initial wave packets, and are not, therefore, based on the PWP approach).

When applying equation (74), it is convenient to restrict the range of initial plane wave packets to those whose momentum composition takes the form

$$A(k_n|\overline{k}_{\rm o}, z_0) = \frac{k_n\hbar^2}{\mu_\lambda} F^n(\overline{k}_{\rm o}, z_0|E) {\rm e}^{-{\rm i}k_n z_0} \tag{84}$$

where $F^n(\overline{k}_o, z_0|E)$ is a real function of E. The phase factor $e^{-ik_n z_0}$ serves to localize the initial plane wave packet about $z = z_0$. From equation (74), this form of $A(k_n|\overline{k}_o, z_0)$ gives

$$\xi_J^{n\kappa}(\mathbf{R}_\lambda, \tilde{\gamma}_\lambda, \tilde{\alpha}_\lambda, r_\lambda|E) = F^n(\overline{k}_o, z_0|E)e^{-ik_n z_0}\,\Psi_J^{n\kappa}(\mathbf{R}_\lambda, \tilde{\gamma}_\lambda, \tilde{\alpha}_\lambda, r_\lambda|E). \tag{85}$$

When using this form of wave packet, it is convenient to define the momentum filter of the probe packets to be of the form

$$A(k_{n'}|\overline{k}_p, q_p) = \frac{ik_{n'}}{4\pi^2}e^{-ik_{n'}q_p} \tag{86}$$

so that

$$g_{n'\kappa'}^{n\kappa}(\theta, E) = F^n(\overline{k}_o, z_0|E)e^{-i(k_n z_0 - k_{n'}q_p)}f_{n'\kappa'}^{n\kappa}(\theta, E). \tag{87}$$

This choice of $A(k_n|\overline{k}_o, z_0)$ and $A(k_{n'}|\overline{k}_p, q_p)$ makes interpreting the DCS particularly straightforward. If one computes the energy-filtered DCS

$$\frac{d\sigma_{n'\kappa'\leftarrow n\kappa}^{FILT}}{d\Omega}(\theta, E) = \left|g_{n'\kappa'}^{n\kappa}(\theta, E)\right|^2 = \left[F^n(\overline{k}_o, z_0|E)\right]^2\frac{d\sigma_{n'\kappa'\leftarrow n\kappa}}{d\Omega}(\theta, E) \tag{88}$$

then one knows that the wave packet and time-dependent DCS describe precisely the dynamics that produces $d\sigma_{n'\kappa'\leftarrow n\kappa}^{FILT}/d\Omega(\theta, E)$. This approach is particularly useful when $F^n(\overline{k}_o, z_0|E)$ has the form of a flat window (such as a wavelet [45]). In this case, $F^n(\overline{k}_o, z_0|E)$ effectively 'cuts out' an interesting energy-region from the DCS, and is then used to generate the plane wave packet and time-dependent DCS that visualize the dynamics in this energy region. We illustrate this approach in section 4.2 below.

Although we recommend that the PWP equations be applied indirectly, there is one instance when it is advantageous to apply the equations directly. This is to obtain the DCS from the wave packet $\chi^{n\kappa}(\mathbf{R}_\lambda, \tilde{\gamma}_\lambda, \tilde{\alpha}_\lambda, r_\lambda|t)$ by performing directly the integration in equation (78), using numerical quadrature. It is worth computing some of the DCSs in this way (for a small number of final states) in order to check that the computed wave packets map correctly on to the DCS.

4.2. *Direct and time-delayed mechanisms in $H + D_2$ and $F + HD$*

To illustrate the above, we review recent applications of the PWP method to the prototypical $H + D_2$ and $F + HD$ reactions. Figure 6 shows snapshots of the time-evolving wave packet computed [1, 8] for the $H + D_2$ ($v = 0, j = 0$) reaction. The packet has been projected on to the $v' = 3$ state of the HD product, and multiplied by a coordinate filter that restricts the projection to the product side of the transition state. The upper and lower halves of the two-dimensional plots in figure 6 are symmetric, because they represent a two-dimensional cut through the three-dimensional scattering, which is cylindrically symmetric about the reagent approach axis. Note that each plot has been multiplied by a factor of $\sin\theta$ (to give a fair representation of the flux per solid angle [8]), and this produces the node along the z-axis.

The wave packets used in figure 6 were computed using the approach of section 4.1. The energy filter $F^n(\overline{k}_o, z_0|E)$ was chosen to be a distributed approximating functional (DAF) [45], which has the flat form shown in figure 7(a). This effectively cuts a section out of the DCS, to produce the filtered DCS $[d\sigma_{n'\kappa'\leftarrow n\kappa}^{FILT}/d\Omega(\theta, E)$ of equation (88)], as illustrated in figure 7(b) for the (00→00) DCS. Following section 4.1, the wave packet of figure 6 represents the dynamics that produces this section of the (00→30) DCS. The full (00→30) DCS is shown in

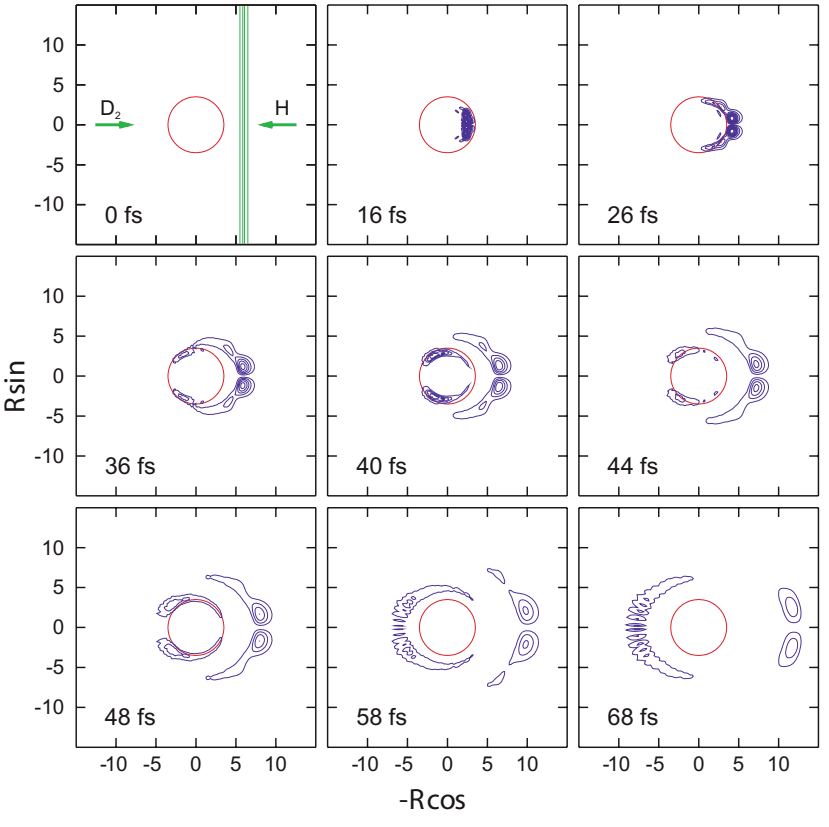

Figure 6. Snapshots from a plane wave packet description of the $H + D_2(v = 0, j = 0) \rightarrow HD + D$ reaction. The contours at times $t > 0$ are obtained by projecting the wave packet on to the $HD(v' = 3, j' = 0)$ rovibrational wave function, taking the square modulus, and multiplying by $\sin\theta$. The contours at time $t = 0$ show the initial $H + D_2$ plane wave packet. The circles are of radius $R = 3.5$ a.u. and give a rough indication of the extent of the transition state region. Two reaction mechanisms are visible, separated by a time delay of about 25 fs. (Reproduced with permission from ref. [1].)

figure 8, together with the time-dependent DCS, which contains the same spread of energies as the wave packet, and illustrates the mapping of the packet on to the cross-section. These results show very clearly that the forward part of the DCS is produced by a time-delayed mechanism, whose product first appears over the transition state at about $t = 35$ fs, in the region of $\theta = 60^\circ$.

Figure 9 shows a similar plot to figure 6, obtained for the $F + HD$ $(v = 0, j = 0)$ reaction [3]. The packet has been projected on to two different quantum states of the HD product (shown in different colours). The spread of energies contained in the packet goes from threshold to about 0.15 eV. The wave packet shows that, even in this low-energy range, the $F + HD$ reaction undergoes four different reaction mechanisms, two direct, and two time-delayed.

This last example illustrates one of the main advantages of the PWP approach. It has the ability to represent clearly different reaction mechanisms, by visualizing their separation in time and scattering direction, and is able to map each mechanism on to the DCS. Below, we will explain how to exploit this last aspect in detail, using

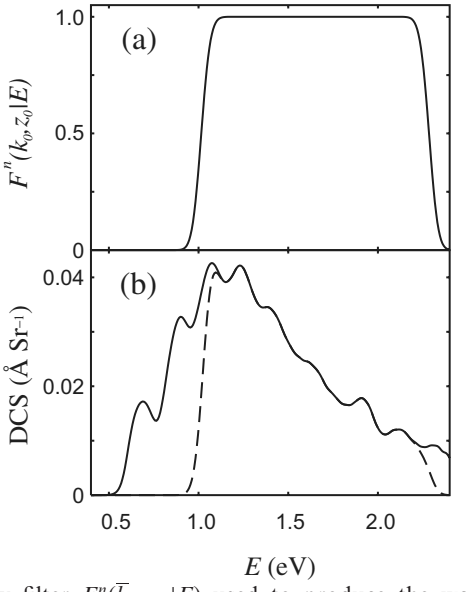

Figure 7. (a) The energy filter $F^n(\bar{k}_o, z_0|E)$ used to produce the wave packet of figure 6. (b) Effect of the energy filter on the DCS. The solid line is the state-to-state DCS $d\sigma_{000\leftarrow000}/d\Omega\,(\theta = 180^\circ, E)$; the dashed line is the corresponding filtered DCS $d\sigma^{FILT}_{000\leftarrow000}/d\Omega\,(\theta = 180^\circ, E)$ of equation (88). (Reproduced with permission from ref. [8].)

time and energy filters to disentangle contributions from different reaction mechanisms in the DCS. By using the language 'reaction mechanism' we are tacitly assuming a semiclassical description of the dynamics, in which different mechanisms occupy different regions of phase space. We know from the success of quasi-classical trajectory (QCT) methods [46] that such a picture is usually valid for reactions. The PWP approach complements the QCT approach, by showing how the dynamics of the mechanisms is changed by quantum effects. For example, the magnitude of the forward-scattered mechanism in $H + D_2$ is about three times greater in the quantum than in the QCT treatment [47], and shows marked interference with the direct mechanism (see below). In $F + HD$, the two time-delayed mechanisms do not appear at all in a QCT calculation (since they are caused by quantum resonances [48]), but the direct mechanisms are well reproduced [49].

We must emphasize that the PWP approach complements, but does not supplant, the standard time-independent quantum and semiclassical methods of analysing the DCS. In fact, use of such methods is essential, in order to obtain as complete a picture as possible of the dynamics. For example, a time-independent analysis on $H + D_2$ [50] showed that the time-delayed mechanism is caused by 'quantized bottleneck states' [51, 52], formed at the adiabatic threshold energies. One can estimate that there are about 30 of these states present (several for each contributing partial wave) in the forward-scattered part of the wave packet. The PWP approach shows how these states superpose, to give one, simple, time-delayed mechanism. It also shows how this mechanism interferes with the direct mechanism (see below). In $F + HD$, time-independent calculations [48, 53] have identified a series of Feschbach resonances (one per partial wave), formed at the reaction threshold.

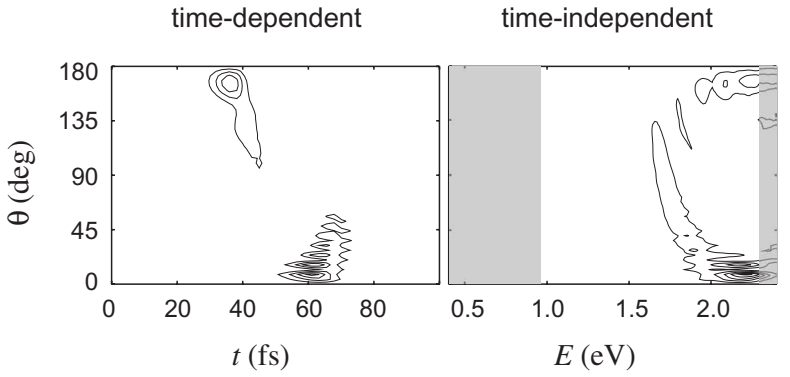

Figure 8. The time-dependent and time-independent DCS, $d\sigma_{300\leftarrow000}/d\Omega(\theta,t)$ and $d\sigma_{300\leftarrow000}/d\Omega(\theta,E)$, corresponding to the wave packet of figure 6. The energies on either side of the filter $F^n(\bar{k}_o,z_0|E)$ (which are not contained in the time-dependent DCS or wave packet) are shaded grey. Both the DCSs in this figure have been multiplied by a factor of $\sin\theta$. (Reproduced with permission from ref. [8].)

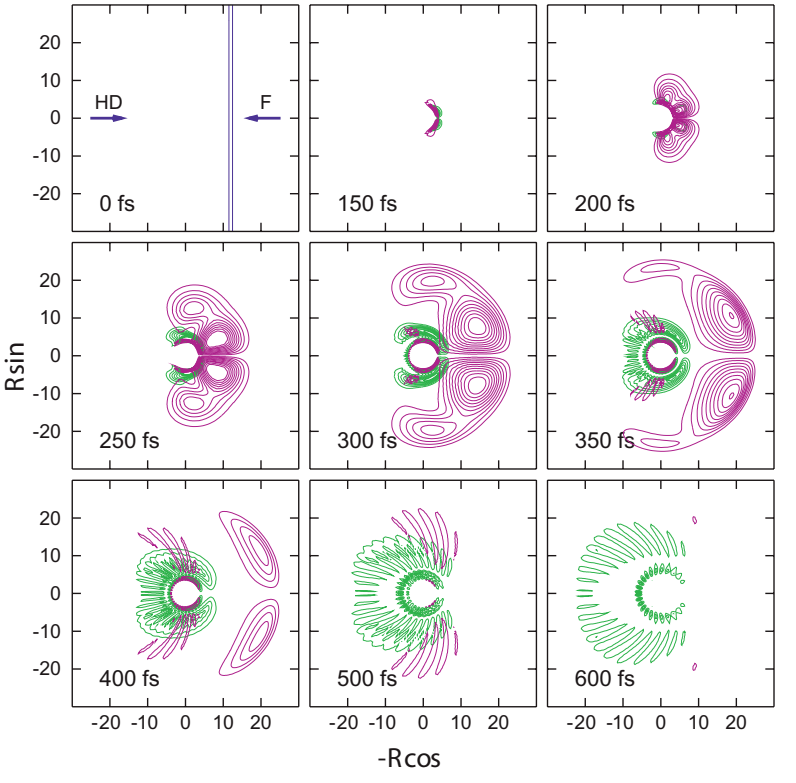

Figure 9. Snapshots from a plane wave packet description of the F + HD ($v=0,j=0$) → HF + D reaction, in the collision energy range $E=0$–0.15 eV. The square modulus of the initial F + HD plane wave packet (blue) is plotted in the 0 fs snapshot. The later snapshots plot the square modulus of the scattered wave packet, projected on to asymptotic HF quantum states ($v'=2,j'=0$) (purple) and ($v'=3,j'=0$) (green). The frame at 300 fs shows clearly the two direct, and the two time-delayed mechanisms. The latter are trapped in two rings, between $R=3.5$–4.0 bohr, and $R=5$–8 bohr. (Reproduced with permission from ref. [3].)

The PWP approach reveals the time-delayed dynamics that result when these resonances superpose.

4.3. *Using time and energy filters to interpret the DCS*

One can obtain new insights from the PWP approach, simply by inspecting wave packets such as those in figures 6 and 9. However, one can often make more detailed analyses, by using the PWP approach to decompose the DCS into contributions from different mechanisms. This is done by applying time and energy filters to the scattering amplitudes, as described below. Such approaches are particularly useful when untangling the effect on the DCS of quantum interference between mechanisms.

4.3.1. *Time filters: interfering direct and time-delayed mechanisms in $H + D_2$*

One thing that is *not* evident in figure 6 is that the time-delayed mechanism has a tail, which extends round into the backward direction. The tail may be visualized by increasing the number of contours in figure 6, or, equivalently, in the time-dependent DCS of figure 8. The latter option is plotted in the centre of figure 10 (taken from Ref. [2]). Since the tail extends back to $\theta = 180^\circ$, one can expect to see effects in the backward-scattered DCS caused by interference of the tail with the direct mechanism.

Reference [2] investigated these effects, as follows. The time-dependent scattering amplitude $f^{n\kappa}_{n'\kappa'}(\theta, t)$ was computed using the approach described in section 4.1, and was then multiplied by two time-filters. The first filter extended from $t = 0$ fs to the cut-line (shown in grey in figure 10), and thus captured the contribution to $f^{n\kappa}_{n'\kappa'}(\theta, t)$ from the direct mechanism. The second filter extended from the cut line to $t = 120$ fs, and thus captured the contribution from the time-delayed mechanism. Both the filtered amplitudes were Fourier-transformed, to produce the DCSs shown at the bottom of figure 10. These are the DCSs that would have been obtained if each mechanism had been able to operate separately, without interfering with the other one. Comparison with the full DCS (top of figure 10) shows that interference between the two mechanisms produces a major effect: there is a series of humps (as a function of E) in the backward direction of the full DCS, which is completely absent from the direct DCS. The humps are present in the time-delayed DCS, but are too small to see clearly in figure 10. Thus quantum interference with the direct mechanism amplifies these humps by an order of magnitude (as in heterodyne light scattering). It is because of this interference that the humps are so pronounced, and can be detected experimentally [54]. Time-independent calculations [54] suggest that the humps are themselves a result of interference, between different quantized bottleneck states in the time-delayed tail.

This approach of applying time filters to $f^{n\kappa}_{n'\kappa'}(\theta, t)$ is likely to be useful whenever direct and time-delayed mechanisms interfere in the DCS. A similar application to the above was made to the F + HD reaction [4], and identified patterns in the DCS caused by interference between the resonant and direct mechanisms.

4.3.2. *Energy filters: probing the $F + HD$ tunnelling resonance*

In addition to using time filters, the DCS can sometimes also be analysed using energy filters. This was demonstrated for the F + HD reaction in ref. [4]. To use energy filters in this way, one has simply to apply the procedure of section 4.1 several times, using different choices of $F^n(\bar{k}_o, z_0|E)$ in equations (84)–(88). In Ref. [4],

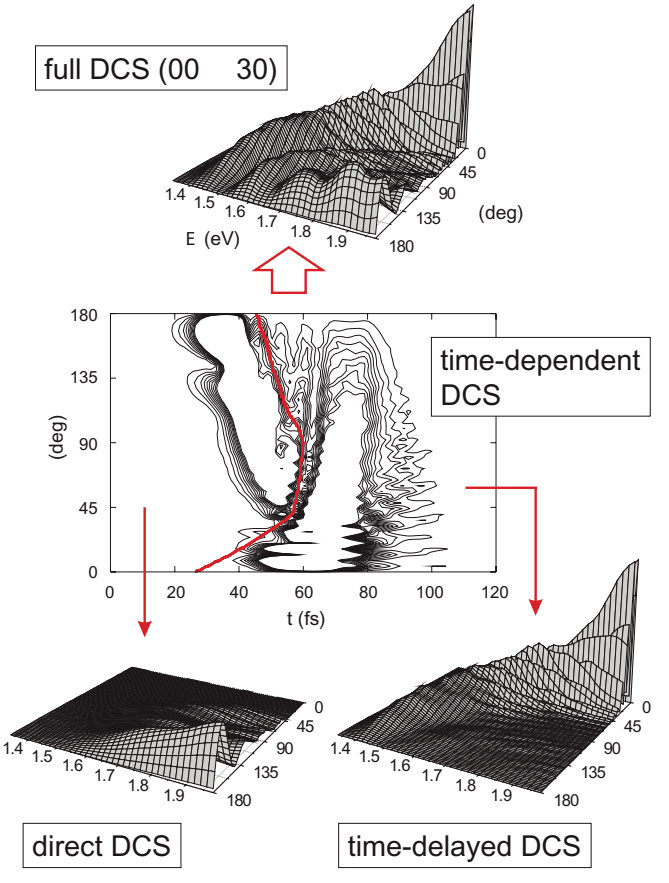

Figure 10. Diagram illustrating the use of time filters to analyse the DCS $d\sigma_{300\leftarrow000}/d\Omega(\theta, E)$ of figure 8. The central plot is a magnified version of $d\sigma_{300\leftarrow000}/d\Omega(\theta, t)$ of figure 8, which shows clearly the backward-scattered tail of the time-delayed mechanism. Time filters [2] are applied to the left and right of the cut-line (grey), to produce separate cross-sections for the direct and time-delayed mechanisms. The series of humps visible in the backward direction come from the time-delayed mechanism, and are magnified approximately sevenfold by quantum interference with the direct mechanism. (Reproduced with permission from ref. [2].)

this procedure was generalized somewhat, by making $F^n(\bar{k}_o, z_0|E)$ J-dependent. A J-dependent filter has the effect of isolating a region in the $E-\theta$ plane from the DCS, and of generating a wave packet that illustrates the scattering into this region.

The main results of the analysis of ref. [4] are reproduced in figures 11 and 12. Figure 11 shows selected state-to-state reaction probabilities. Each probability has a peak, just below the classical threshold for reaction, which is caused by a resonance that is formed by tunnelling, and trapped on the product side of the transition state [48, 53]. It is therefore possible to design J-dependent energy filters, each of which isolates the peak, as shown in figure 11(b). These J-dependent filters were used to construct the time-evolving wave packet shown in figure 12(a). Comparison of this packet with figure 9 confirms that the earlier of the two time-delayed mechanisms is produced by a superposition of the threshold resonance peaks, and that the energy filters have successfully separated out this mechanism from the other three.

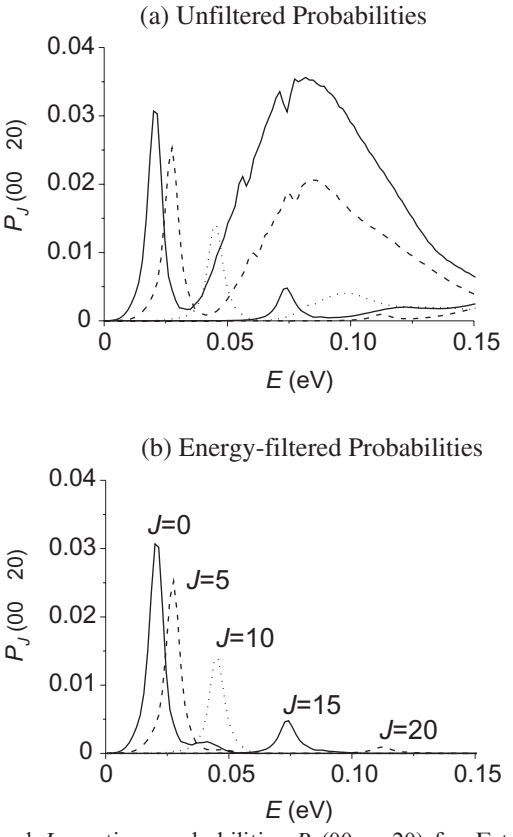

Figure 11. Selected fixed-J reaction probabilities $P_J(00 \rightarrow 20)$ for $F + HD$ $(v=0, j=0) \rightarrow$ HF $(v'=2, j'=0) + D$. The $P_J(00 \rightarrow 20)$ in (a) are unfiltered; the $P_J(00 \rightarrow 20)$ in (b) have been multiplied by J-dependent energy filters in order to isolate the Feshbach resonance peaks. (Reproduced with permission from ref. [4].)

Figure 12(b) illustrates another use of energy filters, which is to produce focused wave packets. It is easy to vary the position of the initial plane wave packet, by changing the value of z_0 in the phase factor of equation (84). Typically, the value of z_0 will be slightly larger than R_0 (the smallest distance at which the interaction potential can be neglected). However, z_0 can also take a value smaller than this; for example, it can be set to a value R_t close to the transition state, on the reagent side. In this particular case, the resulting wave packet corresponds to a plane wave packet that is initially confined to $z > R_0$, where it is rather diffuse (along the z-direction). The packet will then become compact, or 'focused' (along the z-direction) when it reaches $z = -R_t$.

Such a choice of z_0 was used to generate the wave packets shown in figure 12(b). The same J-dependent $F^n(\overline{k}_o, z_0|E)$ was applied as in figure 12(a), but z_0 was set to -3 a.u., in order to focus the wave packet just before it crosses the transition state. The focusing has a drastic effect on the wave packet: it eliminates the spreading that the packet undergoes in figures 9 and 12(a), during the F–HD approach. This spreading is considerable, because the range of translational energies in the packet is close to threshold. The spreading changes with J (because the position of the resonance peak changes), and hence the spreading affects the timing of the scattering.

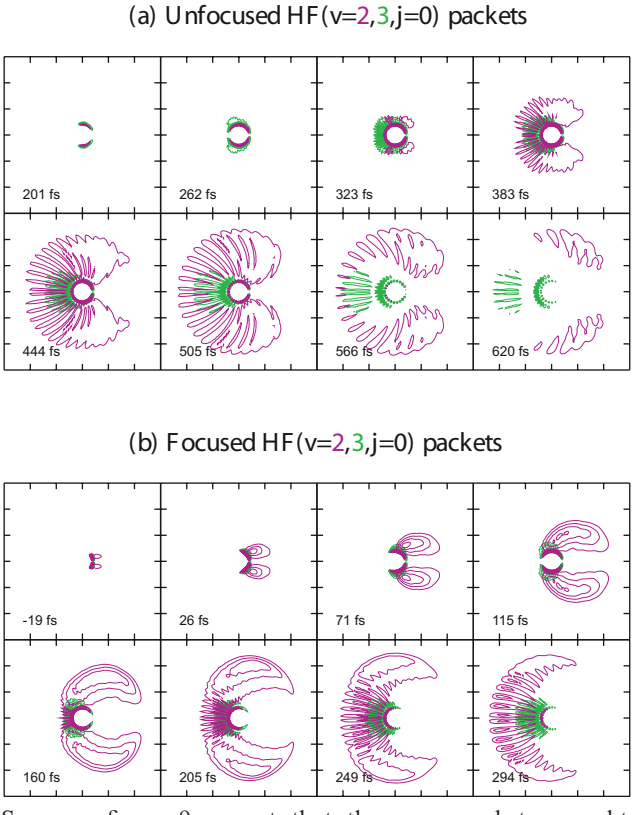

Figure 12. (a) Same as figure 9, except that the wave packet was obtained using the *J*-dependent energy filters illustrated in figure 11. This filtered packet contains mostly just one of the four reaction mechanisms, which is produced by the superposition of Feshbach resonances. (b) Same as (a), except now the wave packet has been focused, so as to remove artifacts caused by spreading of the packet. The resonances superpose to produce a beautiful 'Catherine wheel' rotation. (Reproduced with permission from ref. [4].)

By removing the spreading, the focused packet of figure 12(b) reveals that the resonances produce a 'Catherine wheel', in which the FHD complex rotates through about 180°. It should be emphasized that, despite the difference between figures 12(a) and 12(b), these two wave packets provide equivalent descriptions of the same physical process. Figure 12(b) can be interpreted immediately by eye, whereas to interpret figure 12(a), one must take into account the effects of the spreading.

4.4. *Visualizing the wave packet*

It is a major challenge to represent graphically the time-evolving wave packet which, even in an A + BC reaction, has five dimensions (ignoring the ϕ-dependence). The approach used to generate figures 6, 9 and 12 was to project the wave packet on to the rovibrational states of the isolated diatom. This approach effectively summarizes the detailed description of the dynamics contained in the wave packet: it shows how many mechanisms are present, when, and in which direction, they scatter, and how the mechanisms interfere. By projecting on to a variety of final states, one can check that the projections are not misrepresenting the dynamics. For

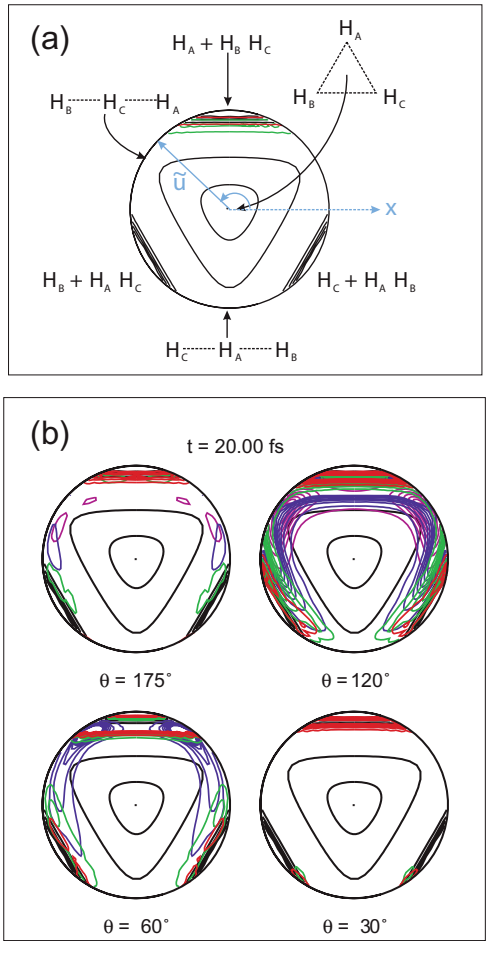

Figure 13. Hyper-spherical coordinate representation of a plane wave packet description of the $H + H_2$ ($v = 0, j = 0$) reaction. (a) Snapshot at $t = 0$, and scattering angle $\theta = 175°$. The coordinates $\tilde{u}$ and α are functions of the hyper-angles [5, 41], and the wave packets are plotted at various values of the hyper-radius ρ [=3.1 (magenta), 3.9 (blue), 4.7 (green), and 5.5 (red) a.u.]. The black contours show the H_3 potential at $\rho = 3.9$ a.u. Various geometries of the three atoms are shown on different parts of the plot. The conical intersection is at the centre. (b) Snapshot at $t = 120$ fs, showing additional scattering angles. (Adapted with permission from ref. [5].)

example, in $F + HD$, it was necessary to project on to two states ($v' = 2$ and $v' = 3$) in order to represent the four mechanisms in this reaction (see figures 9 and 12).

Another approach to representing the wave packet is to show cuts through the wave packet at different scattering angles θ. Such plots give a more detailed picture of the dynamics on the potential energy surface, at the cost of making it less easy to follow the scattering into space of the packet. They should therefore be used in conjunction with projection plots (such as those of figures 6, 9 and 12).

Figure 13 shows cuts at four scattering angles, taken through the wave packet $\chi^{n\kappa}(\mathbf{R}_\lambda, \tilde{\gamma}_\lambda, \tilde{\alpha}_\lambda, r_\lambda | t)$, for the $H + H_2$ reaction. Each cut is plotted using the hyper-spherical coordinates of ref. [41]. The hyper-radius ρ (the overall separation of the

atoms) is fixed at four different values, and the plots show the wave packet as a function of the hyper-angles (the other two internal degrees of freedom, which describe the relative arrangement of the three atoms). Hence these plots represent four of the five degrees of freedom (the degree of freedom not shown is the rotation of the three atoms about the scattering direction). The plots were used to demonstrate that the $H + H_2$ reaction dynamics involves almost no encirclement of the conical intersection, and can therefore not be expected to show large geometric (Berry) phase effects.

5. Outlook and conclusions

The PWP approach interprets differential cross-sections directly in terms of quantum wave packets. It is applicable to the general two-body quantum scattering problem, and complements standard, time-independent approaches. The PWP approach is particularly useful for describing reactions, or other systems, in which the scattering behaves semiclassically, and is thus readily understood in terms of localized wave packet dynamics. Much of the dynamics in such systems can be described well by quasi-classical trajectory (QCT) methods [46], and the PWP approach complements QCT approaches by highlighting difference due to quantum effects. So far, the PWP approach has been applied to a variety of three-atom reactive scattering systems [1–5, 7, 8], and is currently being extended to reactions with four or more atoms.

In these applications, the PWP approach made it possible to identify and isolate different reaction mechanisms, and to map each mechanism on to the differential cross-section. Isolating the mechanisms was straightforward, because they separated cleanly, as a function of time [2, 3], or of energy [4], and could thus be split apart using time or energy filters. It should be possible to generalize this approach, to treat mechanisms that overlap in time or energy. If we assume that different mechanisms occupy different regions of phase space, then it should be possible to isolate each mechanism by applying general phase-space filters to the wave packet. Probably the best way to construct these filters will be to adapt closed-loop control theory [55]. Such techniques would also be applicable to QCT calculations [46], which could be compared with the PWP results to reveal quantum effects.

One can think of the PWP approach as describing the scattering in terms of a hypothetical femtochemistry experiment. Perhaps, in the not too distant future, it will be possible to design real femtochemistry experiments able to study quantum scattering, and hence full bimolecular reactions.[5] Such experiments would measure quantities that would be closely related to the 'time-dependent differential cross-sections' obtained from the PWP approach. However, for the foreseeable future, the most detailed source of data on bimolecular reactions is likely to remain the time-independent reactive scattering experiment. The latest experiments [11–13] can probe the angular scattering in an impressive level of detail, and present a wonderful source of puzzles to be interpreted by theory.

[5]To our knowledge, no femtochemistry experiment has yet been done on a full bimolecular reaction; the closest to such an experiment are the studies of photoinduced reactions in van der Waals molecules; see e.g. [15].

Acknowledgements

Most of the work reviewed here has grown out of the author's interaction with the reaction dynamics community. It is a pleasure to acknowledge constructive discussions with F. Fernández-Alonso, S. K. Gray, J. C. Juanes-Marcos, D. J. Kouri, D. E. Manolopoulos, M. P. de Miranda, E. Wrede, R. N. Zare, and many others. I also acknowledge the award of a University Research Fellowship from the Royal Society, and funding from the UK Engineering and Physical Sciences Research Council.

References

[1] S. C. Althorpe, F. Fernández-Alonso, B. D. Bean, J. D. Ayers, A. E. Pomerantz, R. N. Zare, and E. Wrede, Nature **416**, 67 (2002).
[2] S. C. Althorpe, J. Chem. Phys. **117**, 4623 (2002).
[3] S. C. Althorpe, Chem. Phys. Lett. **370**, 443 (2003).
[4] S. C. Althorpe, J. Phys. Chem. A **107**, 7152 (2003).
[5] J. C. Juanes-Marcos and S. C. Althorpe, Chem. Phys. Lett. **381**, 743 (2003).
[6] J. C. Juanes-Marcos and S. C. Althorpe, Faraday Discuss. **127** (in press).
[7] S. C. Althorpe, Phys. Rev. A **69**, 042702 (2004).
[8] S. C. Althorpe, J. Chem. Phys. (accepted; in press).
[9] A. E. Pomerantz, F. Ausfelder, R. N. Zare, S. C. Althorpe, F. J. Aoiz, L. Bañares and J. F. Castillo, J. Chem. Phys. **120**, 3244 (2004).
[10] F. Ausfelder, A. E. Pomerantz, R. N. Zare, S. C. Althorpe, F. J. Aoiz, L. Bañares and J. F. Castillo, J. Chem. Phys. **120**, 3255 (2004).
[11] F. Fernández-Alonso and R. N. Zare, Ann. Rev. Phys. Chem. **53**, 67 (2002).
[12] P. Casavecchia, Rep. Prog. Phys. **63**, 355 (2000).
[13] K. Liu, Ann. Rev. Phys. Chem. **52**, 139 (2001).
[14] A. Douhal and J. Santamaria (eds), *Femtochemistry and Femtobiology: Ultrafast Dynamics in Molecular Science* (World Scientific, Singapore, 2002).
[15] J. Phys. Chem. **100**, 12701 (1996).
[16] S. C. Althorpe and D. C. Clary, Ann. Rev. Phys. Chem. **54**, 493 (2003).
[17] R. D. Levine and R. B. Bernstein, *Molecular Reaction Dynamics and Chemical Reactivity* (OUP, New York, 1987).
[18] M. Brouard, I. Burak, D. W. Hughes, K. S. Kalogerakis, J. P. Simons and V. Stavros, J. Chem. Phys. **113**, 3173 (2000).
[19] M. L. Goldberger and K. M. Watson, *Collision Theory* (Wiley, New York, 1964).
[20] R. G. Newton, *Scattering Theory of Waves and Particles* (Springer-Verlag, New York, 1982).
[21] M. S. Child, *Molecular Collision Theory* (Academic Press, London, 1974).
[22] D. Neuhauser, M. Baer, R. S. Judson and D. J. Kouri, J. Chem. Phys. **90**, 5882 (1989).
[23] T. Peng and J. Z. H. Zhang, J. Chem. Phys. **105**, 6072 (1996).
[24] S. K. Gray and G. G. Balint-Kurti, J. Chem. Phys. **108**, 950 (1998).
[25] A. J. H. M. Meijer and E. M. Goldfield, J. Chem. Phys. **110**, 870 (1999).
[26] M. Lara, A. Aguado, M. Paniagua and O. Roncero, J. Chem. Phys. **113**, 1781 (2000).
[27] S. C. Althorpe, J. Chem. Phys. **114**, 1601 (2001).
[28] D. H. Zhang, D. Xie, M. Yang and S.-Y. Lee, Phys. Rev. Lett. **90**, 093201 (2003).
[29] S. M. Kingma, M. F. Somers, E. Pijper, G.-J. Kroes, R. A. Olsen and E.-J. Baerends, J. Chem. Phys. **118**, 4190 (2003).
[30] D. J. Kouri and D. K. Hoffman, Few-Body Systems **18**, 203 (1995).
[31] J. N. L. Connor, Phys. Chem. Chem. Phys. **6**, 377 (2004).
[32] A. Taflove and K. R. Umashankar, IEEE Trans. Electromagn. Compat., **25**, 433 (1983).
[33] A. Taflove and S. C. Hagness, *Computational Electrodynamics: The Finite-Difference Time-Domain Method* (Artech House, Boston, 2000), Chapter 8.
[34] D. J. Kouri, Y. Huang, W. Zhu and D. K. Hoffman, J. Chem. Phys. **100**, 3662 (1994).
[35] A. M. Arthurs and A. Dalgarno, Proc. R. Soc. London Ser. A **256**, 540 (1960).
[36] W. H. Miller, J. Chem. Phys. **50**, 407 (1969).

[37] R. T. Pack, J. Chem. Phys. **60**, 633 (1974).
[38] G. C. Schatz and A. Kuppermann, J. Chem. Phys. **65**, 4642 (1975).
[39] R. N. Zare, *Angular Momentum* (Wiley, New York, 1988).
[40] R. T Pack, G. A. Parker, J. Chem. Phys. **87**, 3888(1987).
[41] A. Kuppermann, Chem. Phys. Lett. **32**, 374 (1975).
[42] D. Skouteris, J. F. Castillo and D. E. Manolopoulos, Comput. Phys. Commun. **133**, 128 (2000).
[43] P. Honvault and J.-M. Launay, J. Chem. Phys. **114**, 1057 (2001).
[44] B. K. Kendrick, J. Chem. Phys. **114**, 8796 (2001).
[45] Y. Huang, W. Zhu and D. J. Kouri and D. K. Hoffman, J. Phys. Chem. **98**, 1868 (1994).
[46] F. J. Aoiz, L. Bañares and V. J. Herrero, J. Chem. Soc., Faraday Trans. **94**, 2483 (1998).
[47] F. Fernández-Alonso, B. D. Bean, J. D. Ayers, A. E. Pomerantz, R. N. Zare, L. Bañares and F. J. Aoiz, Angew. Chem. **Int.** Ed. **39** 2748 (2000).
[48] R. T. Skodje, D. Skouteris, D. E. Manolopoulos, S.-H. Lee, F. Dong, K. Liu, Phys. Rev. Lett. **85**, 1206 (2000).
[49] F. J. Aoiz, L. Bañares, V. J. Herrero, V. Sáez Rábanos, K. Stark, H.-J. Werner, J. Chem. Phys. **102**, 9248 (1995).
[50] S. A. Harich, D. Dai, C. C. Wang, X. Yang, S. D. Chao and R. T. Skodje, Nature **419**, 281 (2002).
[51] D. C. Chatfield, S. L. Mielke, T. C. Allison and D. G. Truhlar, J. Chem. Phys. **112**, 8387 (2000).
[52] D. E. Manolopoulos, Nature **419**, 266 (2002).
[53] R. T. Skodje, D. Skouteris, D. E. Manolopoulos, S.-H. Lee, F. Dong, K. Liu, J. Chem. Phys. **112**, 4536 (2000).
[54] D. Dai, C. C. Wang, S. A. Harich, X. Wang, X. Yang, S. D. Chao and R. T. Skodje, Science **300**, 1730 (2003).
[55] R. S. Judson, H. Rabitz, Phys. Rev. Lett. **68**, 1500 (1992).

Appendix

To prove equation (21) we use the approach given in ref. [30] [which gives a very good introduction to the role of time-independent wave packets (TIWPs) in quantum scattering]. Adopting a schematic notation, we write the TIWP $\xi^{jm_j}(\mathbf{R}, \gamma, \alpha|E)$ of equation (20) in the form

$$\xi = \frac{\mathrm{i}}{2\pi} G\chi(0). \tag{89}$$

Here, $G\chi(0)$ denotes the operation upon the initial wave packet of the Green's function corresponding to the hamiltonian H, with boundary conditions consistent with equation (22). The Lippmann–Schwinger equation for G may be written

$$G = G^{\mathrm{PW}} + GVG^{\mathrm{PW}} \tag{90}$$

where G^{PW} is the Green's function corresponding to the hamiltonian H_0 (non-interacting A and BC), and V denotes, schematically, the action of the A–BC interaction potential. Writing

$$\xi^{\mathrm{PW}} = \frac{\mathrm{i}}{2\pi} G^{\mathrm{PW}}\chi(0) \tag{91}$$

and noting that $\Psi^{jm_j}(\mathbf{R}, \gamma, \alpha|E)$ satisfies

$$\Psi = \Psi^{\mathrm{PW}} + GV\Psi^{\mathrm{PW}} \tag{92}$$

we see that equation (21) must be satisfied provided that

$$\xi^{jm_j\,\mathrm{PW}}(\mathbf{R},\gamma,\alpha|E) = \frac{\mu A(k_j|\overline{k}_\mathrm{o},z_0)}{\hbar^2 k_j}\,\Psi^{jm_j\,\mathrm{PW}}(\mathbf{R},\gamma,\alpha|E). \tag{93}$$

To prove the latter relation, we have simply to note that

$$\chi^{jm_j\,\mathrm{PW}}(\mathbf{R},\gamma,\alpha|t) = \chi^{\mathrm{PW}}(z|\overline{k}_\mathrm{o},z_0|t)\,Y_{jm_j}(\gamma,\alpha)\mathrm{e}^{-\mathrm{i}\epsilon_j t/\hbar} \tag{94}$$

where $\chi^{jm_j\,\mathrm{PW}}(\mathbf{R},\gamma,\alpha|t)$ is the time-dependent wave packet which is the time-to-energy Fourier transform of $\xi^{jm_j\,\mathrm{PW}}(\mathbf{R},\gamma,\alpha|E)$. We can then write

$$\xi^{jm_j\,\mathrm{PW}}(\mathbf{R},\gamma,\alpha|t) = \xi^{\mathrm{PW}}(z|\overline{k}_\mathrm{o},z_0|E-\epsilon_j)\,Y_{jm_j}(\gamma,\alpha). \tag{95}$$

Now, $\xi^{\mathrm{PW}}(z|\overline{k}_\mathrm{o},z_0|E-\epsilon_j)$ is identical to a TIWP for a free particle of mass μ, with energy $E-\epsilon_j$. From ref. [30] we know that this TIWP satisfies

$$\xi^{\mathrm{PW}}(z|\overline{k}_\mathrm{o},z_0|E-\epsilon_j) = \frac{\mu A(k_j|\overline{k}_\mathrm{o},z_0)}{\hbar^2 k_j}\mathrm{e}^{\mathrm{i}k_j z} \tag{96}$$

which proves equation (93) and hence equation (21).

To extend the argument above to prove equation (74) for A + BC reactive scattering, one replaces $Y_{jm_j}(\gamma,\alpha)\mathrm{e}^{-\mathrm{i}\epsilon_j t/\hbar}$ in equation (94) by $Y_{j\Omega}(\tilde{\gamma}_\lambda,\tilde{\alpha}_\lambda)\Phi_n(r_\lambda)\mathrm{e}^{-\mathrm{i}\epsilon_n t/\hbar}$, then obtains equation (96), with ϵ_n in place of ϵ_j, and k_n in place of k_j.